

Generation of ELF and ULF electromagnetic waves by modulated heating of the ionospheric F2 region

B. Eliasson,^{1,2} C.-L. Chang,³ and K. Papadopoulos^{1,3}

Received 11 May 2012; revised 2 August 2012; accepted 23 August 2012; published 18 October 2012.

[1] We present a theoretical and numerical study of the generation of extremely low frequency (ELF) and ultra-low frequency (ULF) waves by the modulation of the electron pressure at the F2-region with an intense high-frequency electromagnetic wave. The study is based on a cold plasma Hall-MHD model, including electron-neutral and ion-neutral collisions, which governs the dynamics of magnetostatic waves and their propagation through the ionospheric layers. Magnetosonic waves generated in the F2 region are propagating isotropically and are channeled in the ionospheric waveguide, while shear Alfvén waves are propagating along the magnetic field. To penetrate the ionosphere from the F2 peak at 300 km to the ground, the magnetostatic waves first propagate as magnetosonic or shear Alfvén waves that encounter a diffusive layer from about 150 km to 120 km where the Pedersen conductivity dominates, and then as helicon (whistler-like) mode waves from about 120 km to 80 km where the ions are collisionally glued to the neutrals and the Hall conductivity dominates. By performing numerical simulations and studying the dispersive properties of the wave modes, we investigate the dynamics and penetration of ELF/ULF waves through the ionospheric layers to the ground and along the geomagnetic field lines to the magnetosphere. Realistic profiles of the ionospheric profiles of conductivity and density are used, together with different configurations of the geomagnetic field, relevant for both the high, mid and equatorial latitudes. Some of the results are compared with recent HAARP experiments.

Citation: Eliasson, B., C.-L. Chang, and K. Papadopoulos (2012), Generation of ELF and ULF electromagnetic waves by modulated heating of the ionospheric F2 region, *J. Geophys. Res.*, 117, A10320, doi:10.1029/2012JA017935.

1. Introduction

[2] The propagation of extremely low frequency (ELF) and ultra-low frequency (ULF) electromagnetic waves in the ionospheric duct has been the subject of several observations and theoretical and numerical studies. The guided propagation of MHD waves around the Alfvén speed minimum at the F2 peak was suggested by *Dessler* [1958], and was supported by analysis of Argus 3 data by *Berthold et al.* [1960] and of the naturally occurring pearl pulsations by *Tepley and Landshoff* [1966]. These observations indicated that the waves propagate with the Alfvén speed (700–900 km/s) in the ionospheric duct. *Greifinger and Greifinger* [1968] conducted a theoretical investigation and derived dispersion relations of the guided propagation in the magnetic meridian

of low-frequency hydromagnetic waves in the ionospheric duct. They found that there is a low-frequency cutoff of about 0.4 Hz for nighttime conditions, and an effective high-frequency cutoff for ground-level signals due to an exponential decrease of the transmission coefficient with frequency at high frequencies. This investigation was later extended to include off-meridian propagation [*Greifinger and Greifinger*, 1973]. Numerical studies of Alfvén wave propagation in the ionosphere have been conducted by *Lysak* [1997, 1999], who developed a two-dimensional numerical model to study the propagation of waves in the 1 Hz band in the auroral zone (with vertical geomagnetic field). This model was later extended to three dimensions and to include the Earth's dipole magnetic field [*Lysak and Song*, 2001; *Lysak*, 2004].

[3] Low-frequency waves in the ionosphere, can be excited by lightning discharges [*Greifinger and Greifinger*, 1976; *Uman*, 1987; *Bertheliet et al.*, 2008; *Milikh et al.*, 1995], seismic events [*Hayakawa et al.*, 2006], and ionospheric heating by powerful high-frequency (HF) transmitters [*Rietveld et al.*, 1984, 1987, 1989; *Barr*, 1998; *Papadopoulos et al.*, 1990, 2005]. The injection of ELF electromagnetic waves into the equatorial E-region by ground-based antennas was suggested by *Eliasson and Papadopoulos* [2009], who found that induced strong horizontal currents and related vertical electric fields can be formed in a few kilometers thick

¹Department of Physics and Department of Astronomy, University of Maryland, College Park, Maryland, USA.

²Institute for Theoretical Physics, Ruhr-University Bochum, Bochum, Germany.

³Technology Solutions, BAE Systems, Arlington, Virginia, USA.

Corresponding author: B. Eliasson, Institute for Theoretical Physics, Ruhr-University Bochum, DE-44780 Bochum, Germany. (bengt@tp4.rub.de)

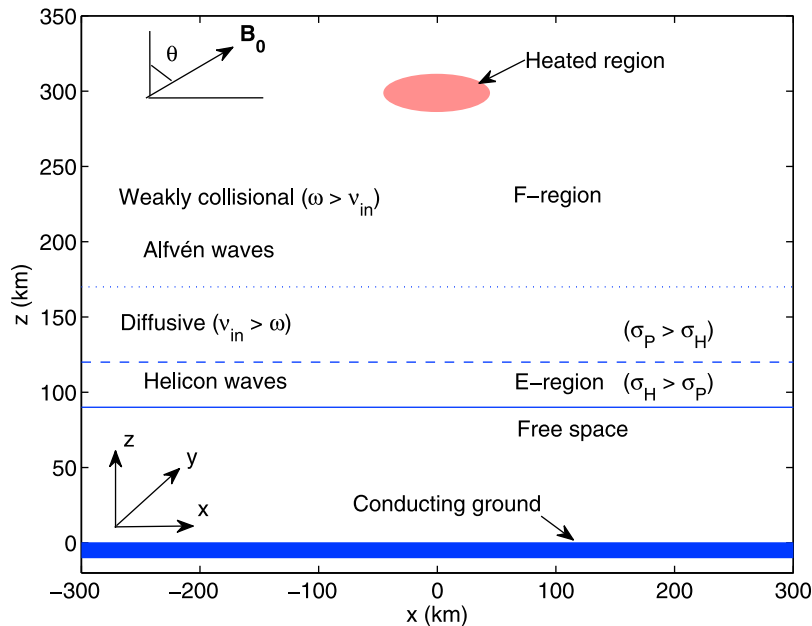


Figure 1. A schematic picture of the ionospheric model.

layer, close to the plasma-free space boundary. This effect is reminiscent of the equatorial electrojet [Forbes and Lindzen, 1976; Forbes, 1981; Rishbeth, 1997; Rastogi, 1989] where a potential drop due to tidal motion along the equatorial line gives rise to an intense electron current by the Cowling effect. The question arises if similar effects can be achieved by magnetosonic waves that are generated at higher altitudes and propagate down to the E-region, and what is the effect of the orientation of the geomagnetic field on the penetration of magnetic fields through the ionospheric layer. Recent theoretical and computational results indicate that modulated F-region HF heating in the polar ionosphere can generate ionospheric currents, via the ionospheric current drive (ICD) process, which act as an antenna to inject magnetosonic waves in the ionospheric plasma [Papadopoulos *et al.*, 2007, 2011a; Papadopoulos, 2009]. The pressure gradient associated with F-region electron heating drives a local diamagnetic current, which triggers a magnetosonic wave. When it reaches the E region of the ionosphere, the electric field of the magnetosonic wave drives Hall currents, which in turn act as a secondary antenna that injects waves into the below Earth-ionosphere waveguide and shear Alfvén waves upwards to the conjugate regions. To address the problem of wave generation and propagation at different latitudes, we here use a cold plasma Hall-MHD model to study numerically the generation of low-frequency electromagnetic waves by the heating of the ionospheric layer for realistic ionospheric parameters and different angles of the geomagnetic field. In addition, the Hall-MHD model takes into account wave frequencies both below and above the ion cyclotron frequency and thus supports electromagnetic cyclotron and whistler waves. The dynamics and penetration of ELF waves through the ionospheric layer to the ground is investigated for different configurations of the geomagnetic field, relevant for high- and mid-latitude facilities such as HAARP in Alaska and Arecibo in Puerto Rico, and for the equatorial region. A simplified analytic model is used to

estimate the spatial attenuation of the waves propagating through the ionosphere.

[4] The paper is organized as follows. In Section 2, we present an ionospheric plasma model, where the Hall MHD equations are put into a matrix form for numerical convenience. Numerical solutions of the model are analyzed in Section 3 for realistic ionospheric profiles and different configurations of the geomagnetic field. The propagation of the waves through the ionospheric layer and down to the plasma-free space boundary to the ground is studied numerically and with a simplified propagation model based on the dispersion relation of the waves. In Section 4, we make some comparisons with recent HAARP experiments where ICD generated ULF/ELF waves were measured on the ground and by the overflying DEMETER satellite. Finally, some conclusions are drawn and future perspectives discussed in Section 5.

2. The Ionospheric Model

[5] We are considering a two-dimensional model in the x - z plane, depicted in Figure 1, where the ionospheric layer is located above $z = z_0 = 90$ km, the atmosphere (free space) below 90 km and the perfectly conducting ground at $z = 0$. The plasma is magnetized by the geomagnetic field \mathbf{B}_0 , which is tilted at an angle θ to the vertical axis. The electron pressure is modulated by a high-frequency radio wave locally in a heated region near the F2 peak at $z = 300$ km, $x = 0$, giving rise to low-frequency electromagnetic waves via the ICD process [Papadopoulos *et al.*, 2011a]. Above about 150–200 km, the plasma is weakly collisional, and the wave frequency ω (corresponding to a few Hz) is larger than the ion-neutral collision frequency ν_{in} . In this region, the dynamics is dominated by magnetosonic and shear Alfvén waves, where the ion mass provides the inertia and the magnetic pressure and tension provide the restoring forces. The shear Alfvén waves propagate primarily along the

geomagnetic field, while the magnetosonic waves propagate isotropically. The F2 peak at 250–300 km is the region of minimum Alfvén speed, which leads to the channeling of magnetosonic waves in the ionospheric waveguide. The plasma between about 150 km and 120 km is dominated by collisions, and both the ions and electrons can be considered inertialess. Here, the ion and electron $\mathbf{E} \times \mathbf{B}_0$ drifts lead to a partial cancellation of the electric current, which results in a diffusive layer where the Pedersen conductivity σ_p dominates the interaction. In the E-layer, at 90–120 km, the ions are collisionally glued to the neutrals, and the dynamics is dominated by the Hall conductivity σ_H due to the electron $\mathbf{E} \times \mathbf{B}_0$ drift. In this region, the whistler branch extends to frequencies below the ion cyclotron frequency and gives rise to weakly damped helicon waves. The ELF waves are partially injected into the neutral atmosphere due to currents in the bottom-side of the E-region [Papadopoulos *et al.*, 2011a]. The propagation of the ELF waves from the source region at 300 km to ground is thus an intricate and interesting problem due to the plasma inhomogeneity and the shifting plasma characteristics at different altitudes.

2.1. Plasma Model

[6] We use a cold plasma Hall-MHD model for the ionosphere, in which the dynamics of the ELF/ULF electromagnetic fields is governed by Faraday's and Ampère's laws

$$\frac{\partial \mathbf{B}}{\partial t} = -\nabla \times \mathbf{E} \quad (1)$$

and

$$\nabla \times \mathbf{B} = \mu_0 en_0(\mathbf{v}_i - \mathbf{v}_e), \quad (2)$$

respectively, where μ_0 is the magnetic vacuum permeability, e is the magnitude of the electron charge, and n_0 is the electron number density. We have neglected the displacement current in equation (2) since the wave speed is much smaller than the speed of light, and have used the quasi-neutrality condition $n_i = n_e = n_0$ for the ion and electron number densities. We are interested in timescales much longer than the lower hybrid oscillation period, so that the electron inertia can be neglected. The dynamics of the plasma is then governed by the inertia-less electron momentum equation

$$0 = -\frac{e}{m_e}(\mathbf{E} + \mathbf{v}_e \times \mathbf{B}_0) - v_{en}\mathbf{v}_e - \frac{\nabla P_e}{m_e n_0} \quad (3)$$

and the ion momentum equation

$$\frac{\partial \mathbf{v}_i}{\partial t} = \frac{e}{m_i}(\mathbf{E} + \mathbf{v}_i \times \mathbf{B}_0) - v_{in}\mathbf{v}_i, \quad (4)$$

where m_e and m_i are the electron and ion masses, v_{en} and v_{in} are the electron-neutral and ion-neutral collision frequencies, and P_e is the externally modulated electron pressure, which provides the source of ELF/ULF electromagnetic waves. The model does not take into account nonlinearities associated with HF wave propagation through the D-region, frequently used to generate ELF and ULF waves by modulating the Polar Electrojet (PEJ) [Rietveld *et al.*, 1984, 1987, 1989; Papadopoulos *et al.*, 1990, 2005; Moore, 2007; Payne *et al.*, 2007]. We have assumed that collisions with neutrals are

dominant. However, for altitudes larger than about 140 km, electron-ion collisions start to dominate over electron-neutral collisions [Forbes, 1981]. We neglect this effect here since the effect of electron collisions on the wave dynamics is negligible at higher altitudes.

[7] For numerical convenience (see Appendix A), the system (1)–(4) is written in the form

$$\frac{\partial \mathbf{A}}{\partial t} = -\mathbf{E} \quad (5)$$

and

$$\frac{\partial \mathbf{E}}{\partial t} = -\omega_{ci}(\Gamma_{in} + \Gamma_{en})\mathbf{E} + \frac{\bar{\epsilon}^{-1}[\nabla \times (\nabla \times \mathbf{A})]}{\mu_0} - \frac{\bar{\mathbf{R}}_e[\nabla \times (\nabla \times \mathbf{E})]}{\mu_0 \tilde{\sigma}} + \left(\omega_{ci} \bar{\mathbf{R}}_i - \frac{\partial}{\partial t} \right) \frac{\nabla P_e}{en_0} \quad (6)$$

where we introduced the vector and scalar potentials \mathbf{A} and ϕ via $\mathbf{B} = \nabla \times \mathbf{A}$ and $\mathbf{E} = -\nabla \phi - \partial \mathbf{A} / \partial t$, using the gauge $\phi = 0$. The $\bar{\mathbf{R}}_e$ and $\bar{\mathbf{R}}_i$ matrices (organizing the vectors as column vectors) are deduced from the electron and ion equations of motion (3) and (4) via the definitions $(\mathbf{v}_e \times \mathbf{B}_0 + m_e v_{en} \mathbf{v}_e) / B_0 \equiv \bar{\mathbf{R}}_e \mathbf{v}_e$ and $(\mathbf{v}_i \times \mathbf{B}_0 + m_i v_{in} \mathbf{v}_i) / B_0 \equiv \bar{\mathbf{R}}_i \mathbf{v}_i$, respectively, as discussed in Appendix A. These matrices are used to construct the inverse of an effective dielectric tensor $\bar{\epsilon}^{-1} = -(\nu_A^2 / \epsilon_0 c^2) \bar{\mathbf{R}}_e \bar{\mathbf{R}}_i$, where $\nu_A = c \omega_{ci} / \omega_{pi}$ is the Alfvén speed, and a conductivity tensor $\bar{\sigma} = \omega_{ci}(\Gamma_{in} + \Gamma_{en}) \bar{\epsilon}$, where we have denoted $\Gamma_{en} = v_{en} / \omega_{ce}$ and $\Gamma_{in} = v_{in} / \omega_{ci}$. Here, $\omega_{ci} = e B_0 / m_i$ and $\omega_{ce} = e B_0 / m_e$ are the ion and electron cyclotron frequencies, $\omega_{pi} = (n_0 e^2 / \epsilon_0 m_i)^{1/2}$ and $\omega_{pe} = (n_0 e^2 / \epsilon_0 m_e)^{1/2}$ are the ion and electron plasma frequencies, and we denoted $\tilde{\sigma} = \epsilon_0 \omega_{pe}^2 / \omega_{ce}$. At the lower boundary between the plasma and free space at $z = z_0 = 90$ km, we have constructed boundary conditions (see Appendix B), by assuming that the x - and y -components of the electric field and vector potential, and their normal derivatives, are continuous. In free space, we have assumed infinite speed of light and that there are no electric charges or currents, while the ground at $z = 0$ is perfectly conducting, so that analytic expressions for the free space electromagnetic fields can be derived (see Appendix B).

2.2. Model Ionospheric Profiles

[8] We use an ionospheric model with realistic parameters and length scales, shown in Figure 2. For the electron/ion number density, we adopt a Chapman profile

$$n_0(z) = n_{\max} \exp(1 - \xi - e^{-\xi}), \quad \xi = \frac{z - z_{\max}}{H}, \quad (7)$$

where we used the maximum number density $n_{\max} = 3.4 \times 10^{11} \text{ m}^{-3}$ at the F2 peak, located at $z_{\max} = 300$ km, and where $H = 120$ km is the ionospheric length scale. The ions are assumed to be singly charged oxygen ions (atomic weight = 16), and the geomagnetic field strength is set to $B_0 = 4 \times 10^{-5}$ T, which gives $\omega_{ci} = 238 \text{ s}^{-1}$ (38 Hz) and $\omega_{ce} = 7.0 \times 10^6 \text{ s}^{-1}$ (1.1 MHz). The maximum of the

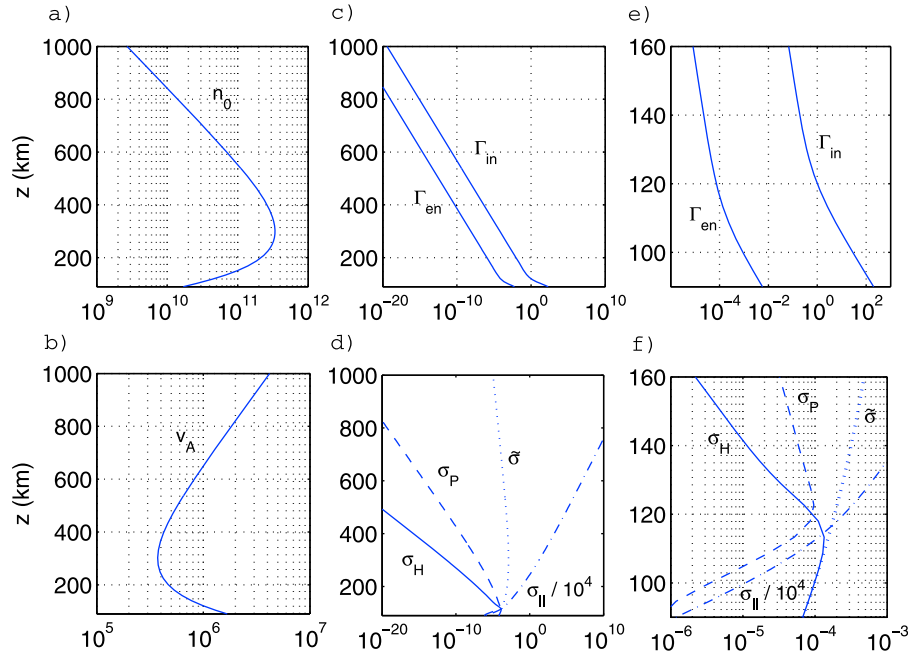


Figure 2. Vertical nighttime profiles of (a) the electron number density n_0 (m^{-3}), (b) the Alfvén speed v_A (m/s), (c) the normalized collision frequencies $\Gamma_{in} = v_{in}/\omega_{ci}$ and $\Gamma_{en} = v_{en}/\omega_{ce}$, and (d) the conductivities σ_H , σ_P , σ_{\parallel} and $\tilde{\sigma}$ (S/m), using the geomagnetic field strength $B_0 = 4 \times 10^{-5}$ T. (e and f) Close-ups of the collision frequencies and conductivities below 160 km.

plasma density at 300 km in Figure 2a corresponds to a minimum of the Alfvén speed in Figure 2b.

[9] The vertical profiles of the normalized electron and ion collision frequencies $\Gamma_{en} = v_{en}/\omega_{ce}$ and $\Gamma_{in} = v_{in}/\omega_{ci}$ are given by

$$\Gamma_{en}(z) = \Gamma_{en0} \left[\exp\left(\frac{z_{en0} - z}{H_{en0}}\right) + \exp\left(\frac{z_{en1} - z}{H_{en1}}\right) \right], \quad (8)$$

and

$$\Gamma_{in}(z) = \Gamma_{in0} \left[\exp\left(\frac{z_{in0} - z}{H_{in0}}\right) + \exp\left(\frac{z_{in1} - z}{H_{in1}}\right) \right], \quad (9)$$

respectively, with $\Gamma_{en0} = 10^{-4}$, $z_{en0} = 110$ km, $H_{en0} = 20$ km, $z_{en1} = 110$ km, $H_{en1} = 5$ km, $\Gamma_{in0} = 0.5$, $z_{in0} = 120$ km, $H_{in0} = 20$ km, $z_{in1} = 120$ km, and $H_{in1} = 5$ km. For these parameters we see in Figure 2e that $\Gamma_{en} \ll 1$ and $\Gamma_{in} \approx 1$ at $z = 120$ km. The density and collision frequency profiles are used to calculate the profiles of the parallel, Pedersen, and Hall conductivity, respectively, from $\sigma_{\parallel} = \tilde{\sigma}(\Gamma_{en}^{-1} + \Gamma_{in}^{-1})$, $\sigma_P = \tilde{\sigma}[\Gamma_{en}/(1 + \Gamma_{en}^2) + \Gamma_{in}/(1 + \Gamma_{in}^2)]$, and $\sigma_H = \tilde{\sigma}[1/(1 + \Gamma_{en}^2) - 1/(1 + \Gamma_{in}^2)]$ (where $\tilde{\sigma} = \varepsilon_0 \omega_{pe}^2 / \omega_{ce} = n_0 e / B_0$). As seen in Figure 2f, $\sigma_P > \sigma_H$ above 120 km, while $\sigma_P < \sigma_H \approx \tilde{\sigma}$ in the E-region below 120 km, where the ions are glued to the neutrals due to collisions.

2.3. Heating Model

[10] We consider a scenario where the F2 peak is heated with a high-frequency, high-intensity radio wave that is amplitude modulated at a low frequency. This leads to Ohmic heating of the electrons and a modulation of the electron pressure $P_e =$

$k_B n_0 T_e$ locally in space, where k_B is Boltzmann's constant and T_e the electron temperature. As a model for the modulated electron pressure gradient, we use $\nabla P_e = n_0 k_B \nabla T_e$, with

$$\nabla T_e = T_{mod} \tanh^2\left(\frac{t}{D_t}\right) \cos(\omega t) \nabla \exp\left[-\frac{x^2}{D_x^2} - \frac{(z - z_{max})^2}{D_z^2}\right], \quad (10)$$

where T_{mod} is the modulation amplitude of the electron temperature, D_{τ} is the rise time, D_x and D_z are the widths of the heated region in the x and z directions, z_{max} is the altitude of the heated region, and ω is the modulation frequency. The gradient of the density at the F2 peak is small and has therefore been neglected, and we have also neglected a rise of the mean electron temperature in the heated region, which will not influence the wave dynamics significantly. The electron pressure gradient enters into the evolution equation (6) for the electric field.

3. Dynamics of ELF Waves Generated in the F2 Region

[11] We present here numerical solutions of equations (5) and (6) for different orientations of the geomagnetic field, using the ionospheric profiles plotted in Figure 2, and the model (10) for the external heating of the electrons.

3.1. Numerical Setup

[12] The simulations are carried out using a computational domain of $-2240 \text{ km} \leq x \leq 2240 \text{ km}$ and $90 \text{ km} \leq z \leq 1020 \text{ km}$ and with $N_x \times N_z = 320 \times 200$ intervals, with spatial grid sizes $\Delta x = 14.0 \text{ km}$ and $\Delta z = 4.67 \text{ km}$. Periodic boundary

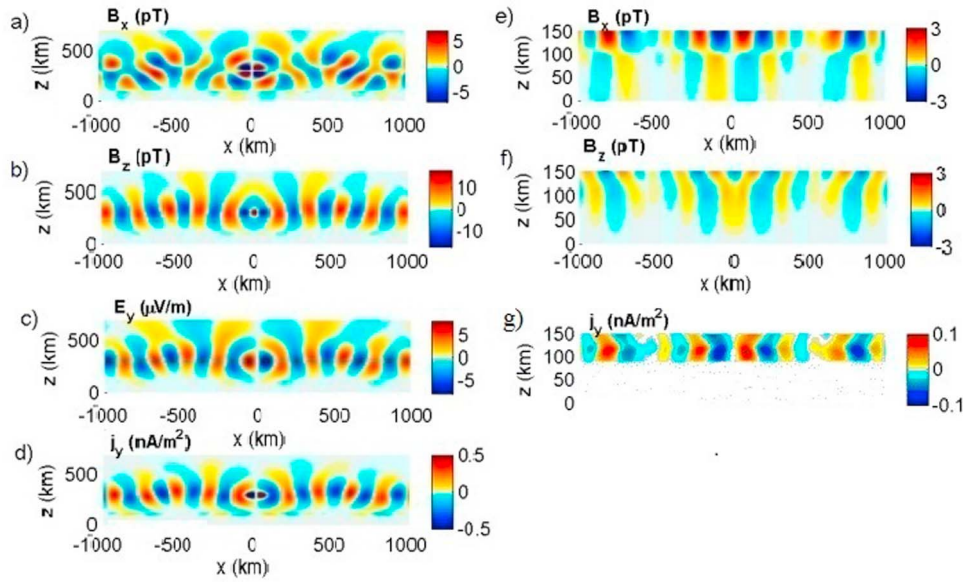


Figure 3. Magnetosonic wave propagation at $t = 5$ s for vertical geomagnetic field ($\theta = 180^\circ$) and the ionospheric profiles in Figure 2, using a source modulation frequency of 2 Hz. (a and b) The x - and z -components of the magnetic field (pT) and (c and d) the associated y -components of the electric field ($\mu\text{V}/\text{m}$) and current density (nA/m^2). (e–g) Close-ups of B_x , B_z and j_y below 150 km and in free space below 90 km.

conditions are used in the x -direction, while a coupling to the free space field is used at the bottom side at $z = 90$ km and first-order outflow boundary conditions are used at the top boundary at $z = 1000$ km; see Appendix B for more details. Pseudospectral methods are used to calculate the x -derivatives and second-order centered difference schemes are for the z -derivatives. The solution is advanced in time using the standard 4th-order Runge-Kutta scheme with a time-step of $\Delta t = 6.25 \times 10^{-5}$ s. The current density in the plasma is obtained from Ampère's law as $\mathbf{j} = \nabla \times (\nabla \times \mathbf{A}) / \mu_0$, while $\mathbf{j} = 0$ in free space below $z = 90$ km. The free space electromagnetic fields are reconstructed analytically, as detailed in Appendix B. In the geometry used here, the z -component of the magnetic field goes to zero at $z = 0$ due to the perfectly conducting ground, and B_y must be identically zero in free space due to the y -component of Ampère's law, $\partial B_y / \partial x = \mu_0 j_z$, which leads to $B_y = 0$ since $j_z = 0$ in free space.

[13] In the heating model (10), we use $T_{mod} = 500$ K, $D_x = 40$ km, $D_z = 20$ km, $z_{max} = 300$ km, $D_t = 0.5$ s, and $\omega = 4\pi\text{s}^{-1}$ (2 Hz).

3.2. Simulation Results

[14] We present below simulations for the cases of vertical, oblique and horizontal magnetic field. The vertical magnetic field case corresponds to experiments performed using the HAARP ionospheric heater in Gakona Alaska [Papadopoulos *et al.*, 2011b] and allows us to compare the results with experimental measurements on the ground and in the ionosphere. The oblique case corresponds to ionospheric heating experiments performed or planned at Arecibo, Puerto Rico and Sura, Russia. The final case corresponds to predictions of a heater located in the dip equator, in places such as Jicamarca, Peru or Tuba, India.

3.2.1. Vertical Magnetic Field: High Latitude Heater

[15] Snapshots of the electromagnetic wave fields for a vertical geomagnetic field, $\theta = 180^\circ$, are shown in Figures 3 and 4, at $t = 5$ s after the transmitter has been turned on. The main features, seen in Figure 3, are magnetosonic waves that

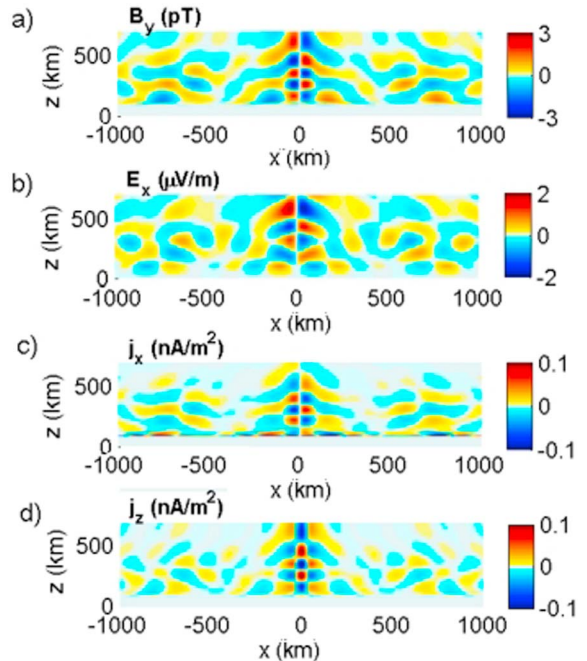


Figure 4. Shear Alfvén wave propagation at $t = 5$ s for vertical geomagnetic field ($\theta = 180^\circ$) and ionospheric profiles given by Figure 2, using a modulation frequency of 2 Hz. The shear Alfvén wave is associated with (a) the y -component of the magnetic field, (b) the x -component of the electric field, and (c and d) the x - and z -components of the current density.

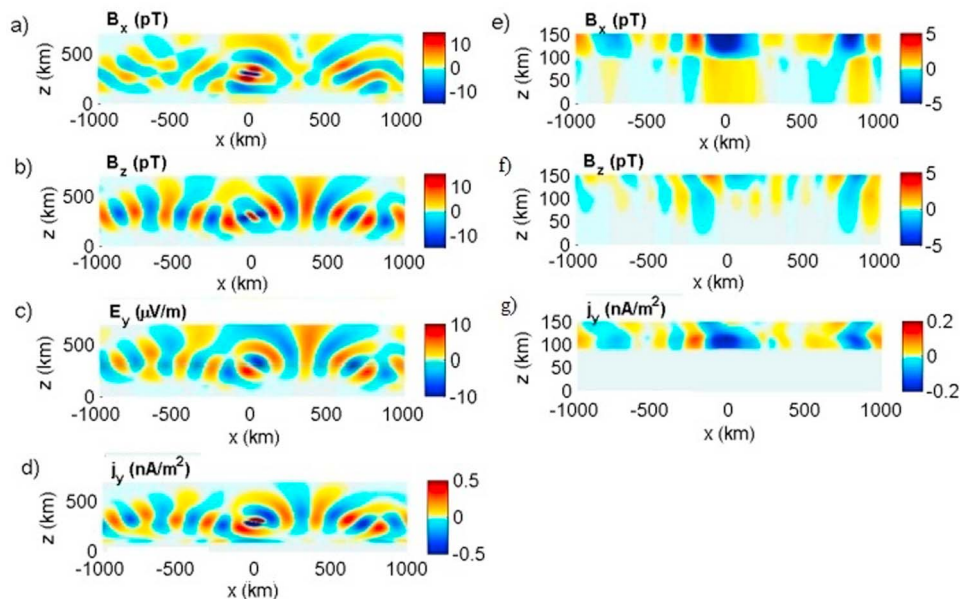


Figure 5. Magnetosonic wave propagation at $t = 5$ s for oblique geomagnetic field ($\theta = 135^\circ$) and the ionospheric profiles in Figure 2, using a source modulation frequency of 2 Hz. (a and b) The x - and z -components of the magnetic field (pT) and (c and d) the associated y -components of the electric field ($\mu\text{V/m}$) and current density (nA/m^2). (e–g) Close-ups of B_x , B_z and j_y below 150 km and in free space below 90 km.

are propagating horizontally in each direction away from the heated region at $x = 0$, at the Alfvén speed minimum at about $z = 300$ km. For the ionospheric profiles in Figure 2, the theoretical Alfvén speed at $z = 300$ km is approximately 4×10^5 m/s (see Figure 2b), which gives a wavelength of about 200 km for 2 Hz, in agreement with Figure 3. The magnetosonic waves are primarily associated with the compression and rarefaction of the total magnetic field, and hence with the z -component of the wave magnetic field and the associated y -components of the electric field and current density. As seen in Figures 3a and 3b, the magnetosonic wave is associated with a wave magnetic field $B_z \approx 10$ pT and electric field $E_y \approx 5$ $\mu\text{V/m}$. Below 150 km, shown in Figure 3d, the structure of the wave magnetic field changes rapidly, and the amplitude decreases by a factor of a few. These changes in the magnetic field are associated with localized currents in the y -direction, visible in Figure 3g.

[16] Smaller amplitude shear Alfvén waves that are propagating vertically along the magnetic field lines are seen in Figure 4. The shear Alfvén waves are associated with the y -component of the magnetic field, the x -component of the electric field and the x - and z -components of the current density. The generation of shear Alfvén waves is due to mode conversion of magnetosonic waves via Hall currents in the E-region [Papadopoulos *et al.*, 2011a], and due to the presence of the Hall term (proportional to $\overline{\mathbf{R}}_e$) in the right-hand side of equation (6). Shear Alfvén waves would not be generated by the modulation of the electron pressure in an ideal MHD model.

3.2.2. Oblique Magnetic Field: Mid-Latitude Heaters

[17] The case of oblique magnetic fields, $\theta = 135^\circ$ is shown in Figures 5 and 6. Figure 5 shows signatures of magnetosonic waves propagating along the ionospheric duct at 300 km and

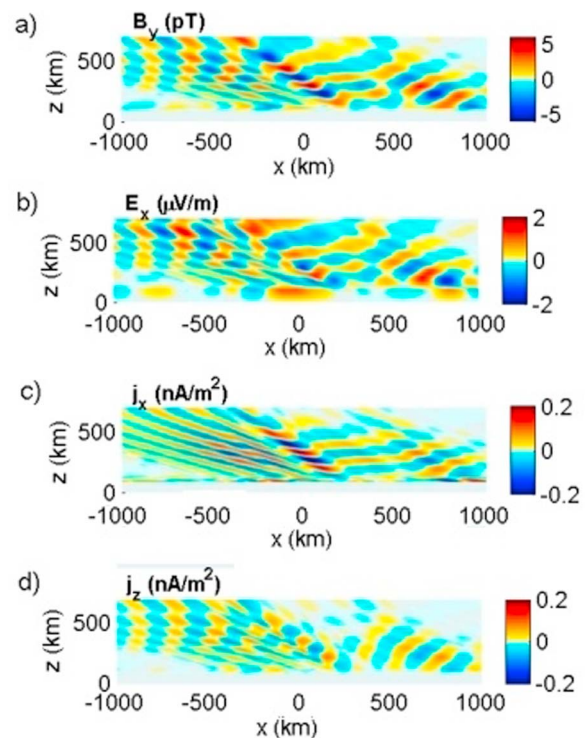


Figure 6. Shear Alfvén wave propagation at $t = 5$ s for oblique geomagnetic field ($\theta = 135^\circ$) and ionospheric profiles given by Figure 2, using a modulation frequency of 2 Hz. The shear Alfvén wave is associated with (a) the y -component of the magnetic field, (b) the x -component of the electric field, and (c and d) the x - and z -components of the current density.

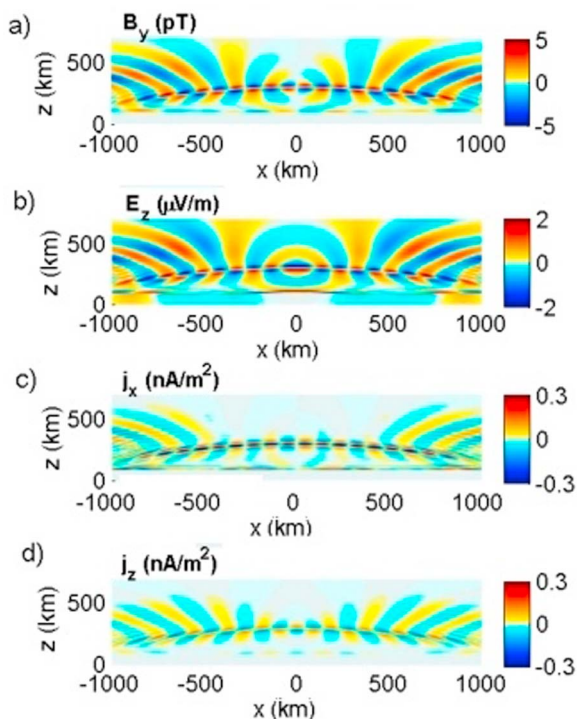


Figure 7. Shear Alfvén wave propagation at $t = 5$ s for oblique geomagnetic field ($\theta = 90^\circ + (x/L) \times 180^\circ/\pi$ and $L = 3000$ km) and ionospheric profiles given by Figure 2, using a modulation frequency of 2 Hz. The shear Alfvén wave is associated with (a) the y -component of the magnetic field, (b) the z -component of the electric field, and (c and d) the x - and z -components of the current density.

carried by the x - and z -components of the magnetic field and the y -components of the electric field and current density. The rapidly changing wave magnetic fields below 150 km in Figure 5e are associated with localized currents in the y -direction, seen in Figure 5g. The shear Alfvén mode, seen in Figure 6, propagates primarily along the geomagnetic field, and is associated with the y -component of the magnetic field and the x - and z -components of the electric field and current density. (Since the electric field parallel to the geomagnetic field is almost zero, we have $E_z \approx E_x$ for $\theta = 135^\circ$, and we therefore show only E_x in Figure 6.)

3.2.3. Horizontal Magnetic Field: Dip-Equator Heaters

[18] Finally, we discuss simulation results with almost horizontal, curved geomagnetic field lines, shown in Figures 7 and 8, which is relevant for projected dip equator heaters. The most striking feature, seen in Figure 7, are the clear signatures of shear Alfvén waves, carried by B_y , E_z , j_x and j_z and propagating in a narrow band along the geomagnetic field lines. The shear Alfvén waves reach the plasma-free space boundary about 1000 km away from the heated region, where they are partially injected into the earth-ionosphere waveguide.

[19] The magnetosonic wave, seen in Figure 8, is associated with a strong compressional x -component of the magnetic field and associated y -components of the electric field and current density. Also visible is the appearance of a thin horizontal current sheath j_y , seen in Figure 8h, associated with a strong vertical electric field E_z , seen in Figure 8g. This effect is similar to the equatorial electrojet, where a weak horizontal electric field E_y , perpendicular to the geomagnetic fields tries to drive a Hall current in the vertical direction. Since current continuity close to the plasma-free space boundary prevents large currents to propagate vertically,

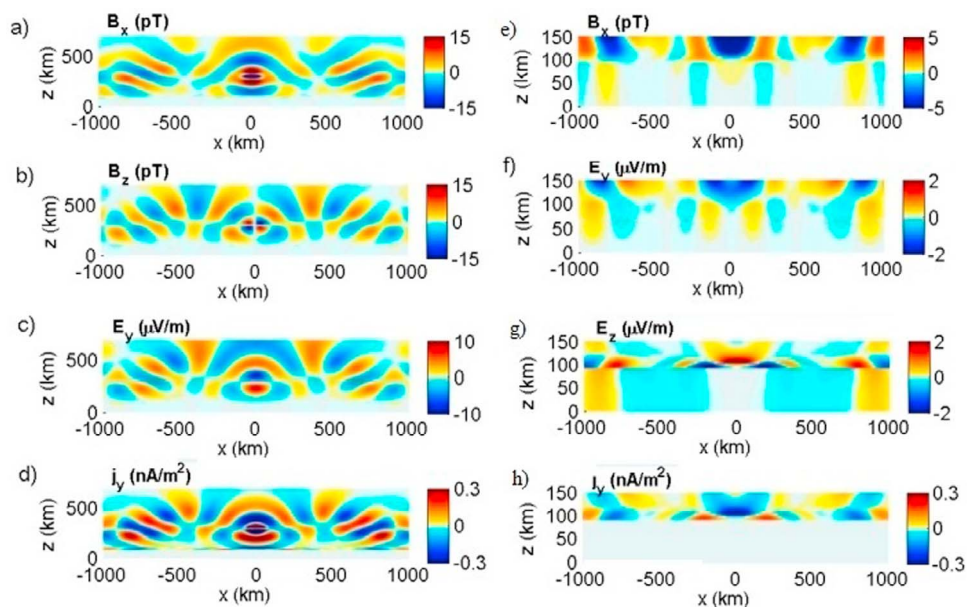


Figure 8. Snapshot of magnetosonic wave propagation at $t = 5$ s for curved geomagnetic field lines ($\theta = 90^\circ + (x/L) \times 180^\circ/\pi$ and $L = 3000$ km), using the ionospheric profiles in Figure 2 and a source modulation frequency of 2 Hz. (a and b) The x - and z -components of the magnetic field (pT) and (c and d) the associated y -components of the electric field ($\mu\text{V/m}$) and current density (nA/m^2). (e–h) Close-ups of B_x , E_y , E_z and j_y below 150 km.

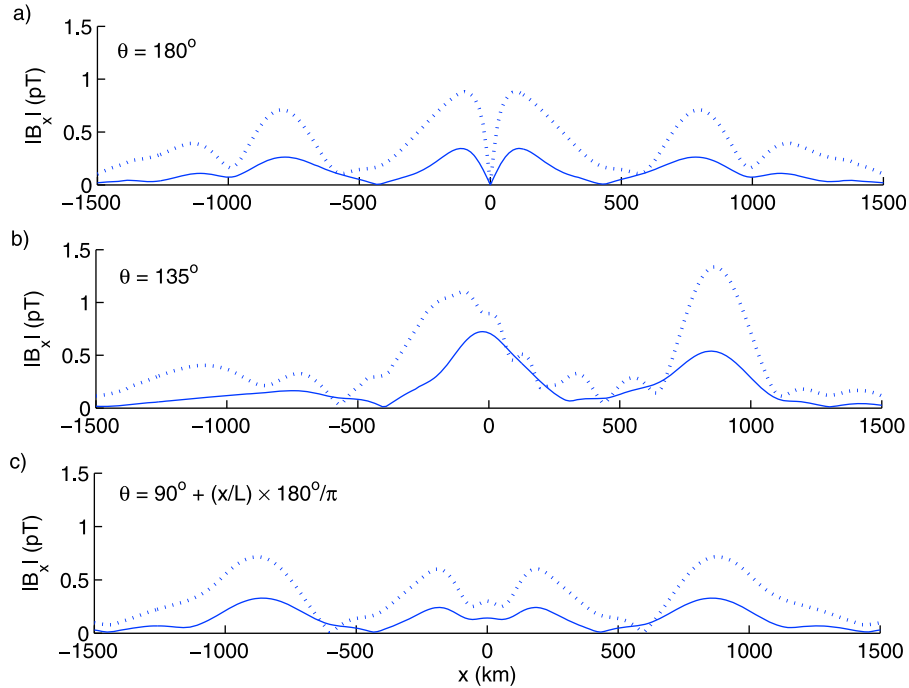


Figure 9. The amplitude of the horizontal magnetic field B_x at the plasma-free space boundary at $z = 90$ km (dotted line) and on ground (solid line) for (a) vertical geomagnetic field $\theta = 180^\circ$, (b) oblique geomagnetic field $\theta = 135^\circ$, and (c) curved geomagnetic field $\theta = 90^\circ + (x/L) \times 180^\circ/\pi$ with $L = 3000$ km.

a large vertical electric field is set up, which in turn drives the intense electron current in the y direction. The resulting Cowling conductivity $\sigma_C = (\sigma_H^2/\sigma_P^2 + 1)\sigma_P$, is a few orders of magnitude larger than the Pedersen conductivity in the E region. For the case when magnetic fields are injected into the ionosphere by a ground-based antenna from below [Eliasson and Papadopoulos, 2009], it was found that the Cowling effect can lead to intense horizontal currents and vertical electric fields in the E-region. For the case considered here, we see in Figure 8h that a sharp drop of the amplitude of B_x at $z \approx 100$ km is associated with the intense current component j_y , via Ampère's law $\partial B_x/\partial z = \mu_0 j_y$, and a large vertical electric field E_z in Figure 8g. The oscillatory current sheet in the E-region could inject electromagnetic waves into the Earth-ionosphere waveguide. Figure 8h shows that the y -component of the current sheet extends about 10 km vertically and 1000 km horizontally in the x -direction with an amplitude of 0.3 nA/m². If we assume that the current sheet also extends 1000 km in the y -direction, we have a dipole moment of about 10^7 Am, which can give significant injection of electromagnetic waves into the earth-ionosphere waveguide.

3.3. Ground Magnetic Field Signatures

[20] For comparison with experiments, where the magnetic field is measured by ground-based magnetometers, the amplitude of the magnetic field leaking down to the ground is calculated from the simulation data. The results are summarized in Figure 9, which shows the amplitude of B_x on the ground and at the plasmas-free space boundary, for the different orientations of the geomagnetic field discussed in Figures 3–8. For the vertical geomagnetic field ($\theta = 180^\circ$),

shown in Figure 9a, there is a minimum at $x = 0$ where the wave magnetic field has a node, while the wave field is significantly larger 30–40 km away from the origin. This skip distance of ICD generated waves has been observed in the high-latitude experiments at HAARP, as discussed in Section 4. The amplitude maxima at $x \approx 100$ km are associated with the shear Alfvén waves that propagate vertically along the magnetic field lines, while the smaller maxima at $x \pm 800$ km are associated with magnetosonic waves that have been guided in the ionospheric duct. For the oblique geomagnetic field ($\theta = 135^\circ$), we see in Figure 9b that there are amplitude maxima somewhat to the left of $x = 0$ and at $x = 800$ km. The wave pattern of B_x and B_z in Figures 5a and 5b indicates that the amplitude maximum to the left of $x = 0$ in Figure 9b corresponds to magnetosonic waves injected almost vertically from the heating region, while the maximum at $x = 800$ km corresponds primarily to magnetosonic waves that have been injected obliquely and reflected from the upper ionospheric layer with higher Alfvén speed above the F2 peak. Finally, for the case of almost horizontal, curved magnetic field, shown in Figure 9c, the amplitude maxima at $x = \pm 100$ km are due to large amplitude magnetosonic waves excited in the heated region, as seen in Figure 8, while the amplitude is somewhat smaller at $x = 0$. The amplitude maxima at $x = \pm 800$ km correspond primarily to magnetosonic waves that have been injected obliquely and reflected from the upper ionospheric layer with higher Alfvén speed, seen in Figures 8a and 8b.

3.4. Transition and Propagation of ELF/ULF Waves Through the Ionospheric Layers

[21] In order to understand the propagation of ELF and ULF waves through the ionospheric layers down to the

neutral atmosphere, we use a simplified model that estimates the spatial attenuation of the wave amplitude along the propagation path. In this model, a plane wave is launched at 300 km and is propagating down to the plasma-free space boundary at 90 km. The relative amplitude for waves propagating vertically is estimated as $\exp\left[-\left|\int_{z_1}^z k_I(z) dz\right|\right]$, where the spatial attenuation rate k_I is obtained from the dispersion relation of the wave with the assumption that the ionospheric profile is slowly varying in comparison with the wave, and z_1 is the altitude of the source of the wave ($z_1 = 300$ km in our case). The dispersion relation is obtained by Fourier analyzing the system (5) and (6) in space and time, by assuming, for example, that the geomagnetic field is directed along the x -axis and that \mathbf{A} and \mathbf{E} are proportional to $\exp(ik_{\parallel}x + ik_{\perp}z - i\omega t)$. This yields the dispersion relation

$$X^2 - Xv_A^2 \left[(k^2 + k_{\parallel}^2) a_{22} + k_{\perp}^2 a_{11} \right] + v_A^4 \left[k^2 k_{\parallel}^2 (a_{22}^2 + a_{23}^2) + k^2 k_{\perp}^2 a_{11} a_{22} \right] = 0, \quad (11)$$

where we have denoted $X = \omega[\omega + i\omega_{ci}(\Gamma_{in} + \Gamma_{en})]$ and $k^2 = k_{\parallel}^2 + k_{\perp}^2$, and a_{ij} are given by $a_{11} = \Gamma_{in}\Gamma_{en} - i(\omega/\omega_{ci})\Gamma_{en}$, $a_{22} = 1 + \Gamma_{in}\Gamma_{en} - i(\omega/\omega_{ci})\Gamma_{en}$, and $a_{23} = \Gamma_{in} - \Gamma_{en} - i\omega/\omega_{ci}$. In addition to the roots of equation (11), we also have solutions given by $X = 0$, which are non-propagating and hence do not contribute to the wave dynamics. We next define $k_{\perp} = k \sin(\theta)$ and $k_{\parallel} = k \cos(\theta)$, where $\theta = 0^\circ$ corresponds to parallel propagation and $\theta = 90^\circ$ corresponds to perpendicular propagation to the magnetic field lines. Inserted into equation (11), this gives

$$X^2 - Xv_A^2 k^2 [(1 + \cos^2(\theta))a_{22} + \sin^2(\theta)a_{11}] + v_A^4 k^4 [\cos^2(\theta)(a_{22}^2 + a_{23}^2) + \sin^2(\theta)a_{11}a_{22}] = 0. \quad (12)$$

The spatial attenuation is now obtained by assuming that the wavenumber is complex, $k = k_R + i k_I$, where k_R is the real wavenumber and k_I the spatial attenuation rate, while the wave frequency ω is real, and by solving equation (12) for k .

[22] It is illustrative to discuss some limiting cases of equation (11). In the collisionless limit $\Gamma_{in} = \Gamma_{en} = 0$, we have $X = \omega^2$, $a_{11} = 0$, $a_{22} = 1$, and $a_{23} = -i\omega/\omega_{ci}$, which inserted into equation (11) gives the dispersion relation for the collisionless shear Alfvén and magnetosonic waves,

$$(\omega^2 - v_A^2 k^2) (\omega^2 - v_A^2 k_{\parallel}^2) - \frac{\omega^2}{\omega_{ci}^2} v_A^4 k^2 k_{\parallel}^2 = 0. \quad (13)$$

[23] For parallel propagation $k = k_{\parallel}$, we have from (13)

$$\omega^2 \mp v_A^2 k_{\parallel}^2 \frac{\omega}{\omega_{ci}} - v_A^2 k_{\parallel}^2 = 0 \quad (14)$$

for the whistler (upper sign) and ion cyclotron (lower sign) branches of the shear Alfvén wave. For parallel propagation along the magnetic field lines, $k_{\perp} = 0$ and $k = k_{\parallel}$, equation (11) yields $X - v_A^2 k_{\parallel}^2 (a_{22} \mp i a_{23}) = 0$, or

$$\omega^2 + \left[(i\Gamma_{en} \mp 1) v_A^2 k_{\parallel}^2 + i\omega_{ci} (\Gamma_{in} + \Gamma_{en}) \right] \frac{\omega}{\omega_{ci}} - [1 + \Gamma_{en}\Gamma_{in} \pm i(\Gamma_{in} - \Gamma_{en})] v_A^2 k_{\parallel}^2 = 0. \quad (15)$$

for the right-hand circularly polarized helicon/whistler (upper sign) and left-hand circularly polarized ion cyclotron (lower sign) branches of the shear Alfvén wave. On the other hand, assuming perpendicular propagation to the magnetic field lines, $k_{\parallel} = 0$ and $k = k_{\perp}$, equation (11) yields the two solutions $X - v_A^2 k_{\perp}^2 a_{22} = 0$ and $X - v_A^2 k_{\perp}^2 a_{11} = 0$. Setting $X - v_A^2 k_{\perp}^2 a_{22} = 0$ yields the dispersion relation for damped magnetosonic waves,

$$\omega^2 + i[(\Gamma_{in} + \Gamma_{en})\omega_{ci}^2 + \Gamma_{en}v_A^2 k_{\perp}^2] \frac{\omega}{\omega_{ci}} - (1 + \Gamma_{en}\Gamma_{in})v_A^2 k_{\perp}^2 = 0, \quad (16)$$

which recovers the magnetosonic mode $\omega^2 = v_A^2 k_{\perp}^2$ in the limit $\Gamma_{en} = \Gamma_{in} = 0$. Setting instead $X - v_A^2 k_{\perp}^2 a_{11} = 0$ gives strongly damped modes.

[24] The right-hand circularly polarized shear Alfvén waves lie on the same dispersion curve as the helicon waves, and connects smoothly to the collisionless shear Alfvén wave for $\lambda_i k_{\parallel} \gg \Gamma_{in}$, where $\lambda_i = c/\omega_{pi}$ is the ion inertial length. For the strongly collisional cases $\lambda_i k_{\parallel} < \Gamma_{in}/2$, the frequency almost exactly obeys the helicon wave dispersion relation $\omega = v_A^2 k_{\parallel}^2 / \omega_{ci}$. Hence, by studying the dispersion relation (15) numerically, we found the following rule of thumb

$$\begin{aligned} \lambda_i k_{\parallel} < \frac{\Gamma_{in}}{2} &\rightarrow \text{helicon waves} \\ \lambda_i k_{\parallel} \gg \Gamma_{in} &\rightarrow \text{shear Alfvén/whistler waves.} \end{aligned}$$

[25] The shear Alfvén waves become more damped for increasing ion-neutral collision frequency, while helicon waves become less damped for increasing ion-neutral collision frequency. The helicon waves are weakly damped for $\Gamma_{in} \gg 1$, since then the Hall conductivity dominates over the Pedersen conductivity, but become strongly damped for $\Gamma_{in} \lesssim 1$, when the Pedersen conductivity dominates. These features are clearly seen in Figure 10a, where we have solved equation (15) for complex wavenumbers $k_{\parallel} = k_R + i k_I$ for different values of the wave frequency $\omega = 2\pi f$, and have used the model ionospheric profiles in Figure 2 to produce profiles of the spatial attenuation rate k_I as a function of altitude. The attenuation rate has a strongly peaked maximum at around 120 km, which is the Pedersen conductivity dominated layer, and decreases rapidly both above and below this altitude. Below 110 km, we have weakly damped helicon waves, and above 150 km, we have weakly damped shear Alfvén waves. The decrease of the amplitude in the propagation from $z_1 = 300$ km is estimated as $\exp\left[-\left|\int_{z_1}^z k_I(z), d, z\right|\right]$, and is plotted in Figure 10b. Above the altitude where $\omega = \Gamma_{in} \omega_{ci} = v_{in}$, the dynamics is dominated by the polarization current which gives rise to the Alfvén waves. For the ionospheric profiles in Figure 2, this altitude is 165 km for 2 Hz, 130 km for 10 Hz and 115 km for 50 Hz. Hence, as seen in Figure 10b, waves with higher frequencies can penetrate the plasma to lower altitudes as weakly damped Alfvén waves, and waves with large enough frequencies can connect directly to the weakly damped helicon waves below 120 km, where the dynamics is dominated by the Hall current. This leads to an increase of the relative amplitude at 90 km for frequencies larger than about

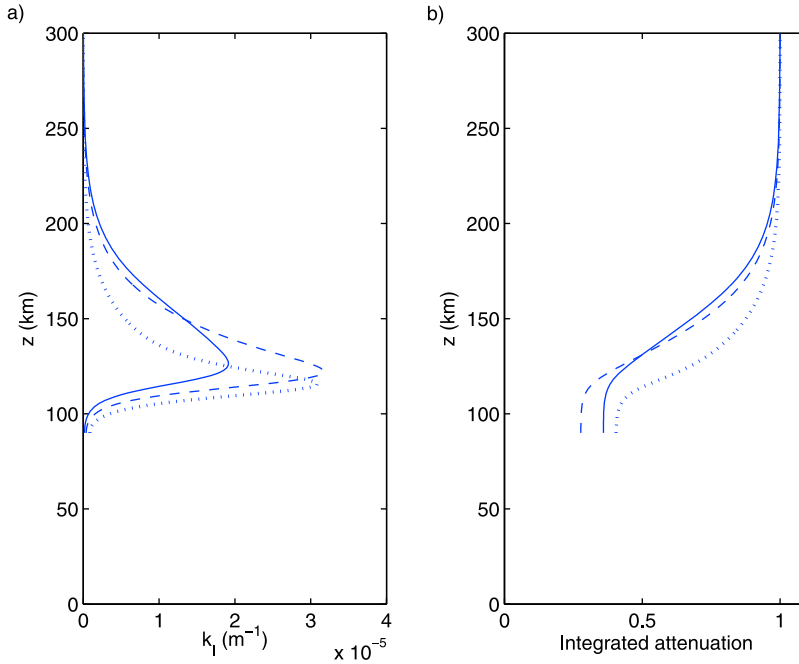


Figure 10. (a) The vertical profiles of the spatial attenuation rate $k_I(z)$ and (b) the integrated spatial attenuation $\exp\left[-\left|\int_{z_1}^z k_I(z'), d, z'\right|\right]$ of a right-hand polarized shear Alfvén wave excited at $z_1 = 300$ km, and propagating parallel to the geomagnetic field lines, for $f = 2$ Hz (solid lines), $f = 10$ Hz (dashed lines) and $f = 50$ Hz (dotted lines).

10 Hz. The increase in amplitude for low frequencies below 10 Hz is due to that the penetration through the Pedersen layer is diffusive with the diffusion coefficient $D \approx 1/(\mu_0 \sigma_P)$. Hence the skin depth for wave penetration can be estimated as $\lambda \sim 1/\sqrt{\mu_0 \omega \sigma_P}$, which increases for decreasing ω .

[26] In Figure 11, we investigate the propagation of left-hand polarized waves along the geomagnetic field lines through the ionospheric layer. For large wavenumbers, they converge to the ion cyclotron resonance and at small wavenumbers to the shear Alfvén waves. However, in contrast to the right-hand polarized wave, they do not have a weakly damped “helicon” mode at large ion-neutral collision frequencies. Using the ionospheric profiles in Figure 2, the spatial attenuation rate and integrated spatial attenuation are plotted in Figures 11a and 11b, and predict a higher degree of damping for the left-hand polarized waves compared to the right-hand polarized waves in Figure 10. Left-hand polarized waves with frequencies above the ion cyclotron frequency 38 Hz are non-propagating, and are therefore not shown in Figure 11.

[27] For applications to the equatorial ionosphere, it is also interesting to investigate the propagation of magnetosonic waves perpendicular to the geomagnetic field lines. Solutions of equation (16) are plotted in Figure 12. The spatial attenuation rate (as well as the real wavenumber) increases with increasing values of Γ_{in} . As seen in Figure 12, the magnetosonic waves become strongly attenuated once they enter the E-region at $z \approx 120$ km, where $\Gamma_{in} \gtrsim 1$, and their relative amplitudes quickly become vanishingly small before reaching the plasma-free space boundary.

[28] Since the magnetosonic wave and the right-hand polarized whistler mode wave lie on the same dispersion surface with different propagation directions to the geomagnetic field lines, it is interesting to investigate the spatial attenuation rate at oblique angles to the geomagnetic field lines. In Figure 13a, we have plotted the integrated spatial attenuation $\exp\left[-\left|\int_{z_1}^{z_0} k_I(z'), d, z'\right|\right]$, of a plane wave generated at $z_1 = 300$ km, which has propagated vertically down to $z_0 = 90$ km. The main result is that there is a strong attenuation of (magnetosonic) waves propagating exactly perpendicularly to the magnetic field (corresponding to $\theta = 90^\circ$). This can be seen in Figure 13a where the waves are moderately attenuated for $\theta = 0^\circ$ (helicon/whistler waves) and $\theta = 45^\circ$, while for $\theta = 90^\circ$, the wave is strongly attenuated except at frequencies below 1 Hz. As seen in Figure 13b, the angular dependence of the integrated spatial attenuation is very different for the low frequency 2 Hz and the higher frequencies 10 Hz and 50 Hz. The 2 Hz signal is strongly attenuated only in an angular interval of a few degrees around the purely perpendicular propagation, which indicates that the reason for the amplitude maxima at $x = \pm 100$ km in Figure 9c, is that the magnetosonic wave has propagated obliquely (not exactly perpendicularly) to the geomagnetic field lines through the ionosphere down to the plasma-free space boundary. Waves with frequencies 10 Hz and 50 Hz are strongly attenuated in an interval of about $\pm 20^\circ$ from perpendicular propagation. At $\theta = 90^\circ$ the integrated spatial attenuation is $\sim 10^{-2}$, 10^{-3} and 10^{-8} , respectively, for frequency 2 Hz, 10 Hz and 50 Hz. Hence, one

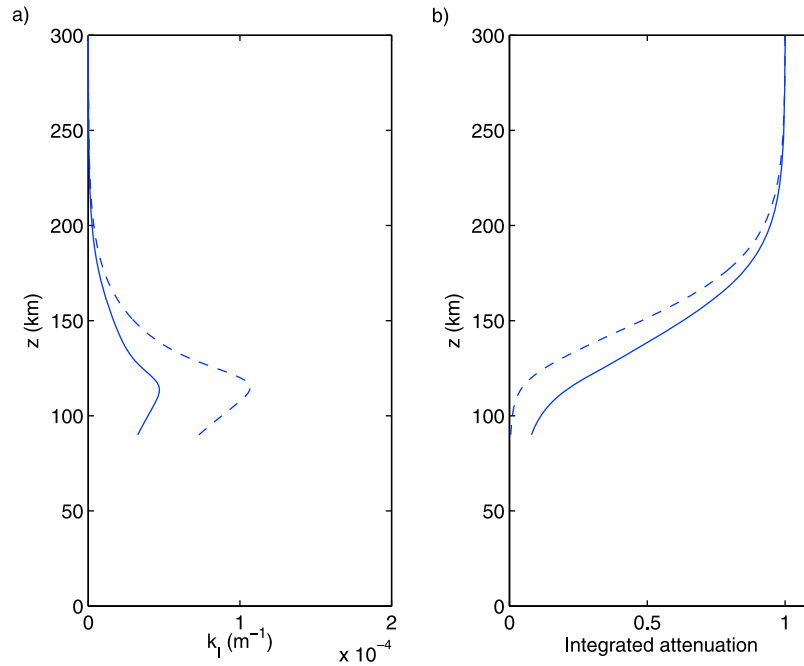


Figure 11. (a) The vertical profiles of the spatial attenuation rate $k_I(z)$ and (b) the integrated spatial attenuation $\exp\left[-\left|\int_{z_1}^z k_I(z), d, z\right|\right]$ of a left-hand polarized shear Alfvén/ion cyclotron wave excited at $z_1 = 300$ km, and propagating parallel to the geomagnetic field lines, for $f = 2$ Hz (solid lines) and $f = 10$ Hz (dashed lines). For frequencies above the ion cyclotron frequency $f_{ci} = 38$ Hz, the wave mode becomes non-propagating and strongly damped.

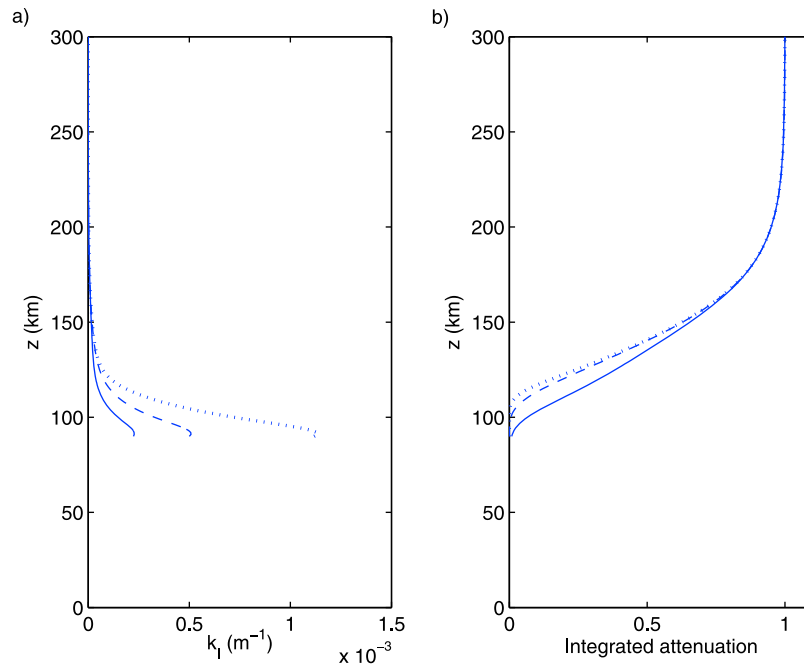


Figure 12. (a) The vertical profiles of the spatial attenuation rate $k_I(z)$ and (b) the integrated spatial attenuation $\exp\left[-\left|\int_{z_1}^z k_I(z), d, z\right|\right]$ of a magnetosonic wave excited at $z_1 = 300$ km, and propagating perpendicular to the geomagnetic field lines, for $f = 2$ Hz (solid line), $f = 10$ Hz (dashed line) and $f = 50$ Hz (dotted line).

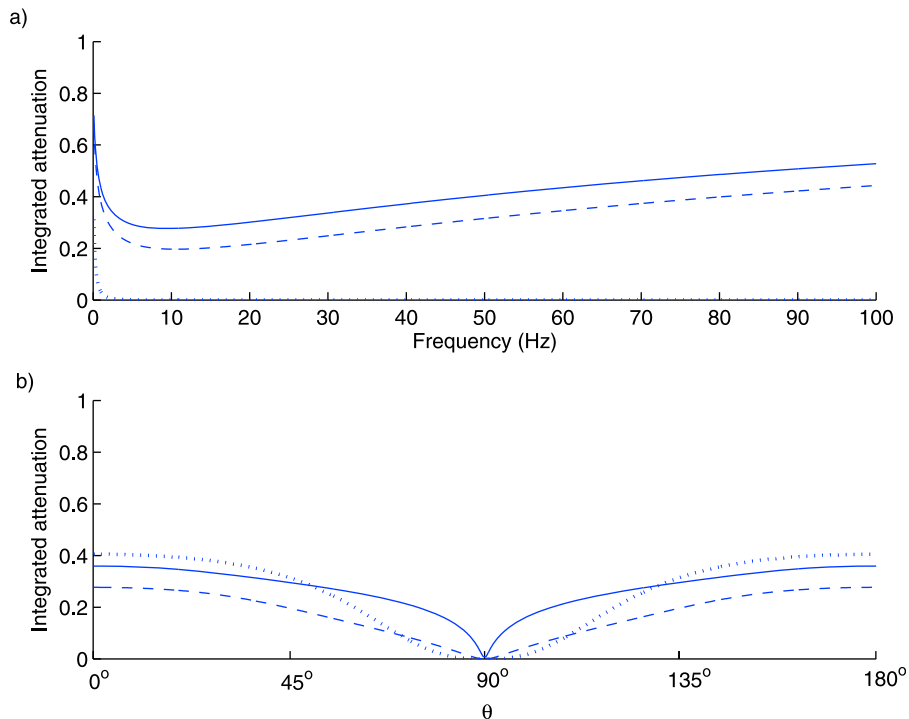


Figure 13. The integrated spatial attenuation $\exp\left[-\left|\int_{z_1}^{z_0} k_I(z_i), d, z\right|\right]$ at the bottom-side ionosphere $z_0 = 90$ km for a plane wave excited at $z_1 = 300$ km, (a) as a function of frequency for $\theta = 180^\circ$ (solid line), $\theta = 135^\circ$ (dashed line) and $\theta = 90^\circ$ (dotted line), and (b) as a function of θ for wave frequency 2 Hz (solid line), 10 Hz (dashed line) and 50 Hz (dotted line). The low frequency wave 2 Hz is strongly attenuated in a narrow region around $\theta = 90^\circ$, corresponding to perpendicular propagation to the geomagnetic field lines.

would expect that there is an effective high-frequency cutoff of the signal around approximately 5–10 Hz measured on ground in the equatorial region for ULF waves generated at the vertically overhead F2 peak.

[29] Finally, it is worth noting that a significant amount of absorption of the HF electromagnetic wave also can occur in the D-region ionosphere below 90 km, where the product of the electron density and the electron-neutral collision frequency has a maximum. This effect is not accounted for by the present model, where the modulated electron pressure is assumed to be an external source.

4. Some Experimental Results

[30] While the emphasis on the paper was the theoretical modeling of ICD in general and its properties as a function of the geomagnetic latitude of the heater, we present in this section specific results of ICD experiments that relate to features demonstrated in the modeling. The most comprehensive set of experiments were conducted using the HAARP ionospheric heater in Gakona, Alaska and some of the ground measurements were reported by *Papadopoulos et al.* [2011b]. There are also two experimental results from mid-latitude heaters, one using the Arecibo heater [*Ganguly et al.*, 1986] that was subsequently destroyed by floods and a recent one using the Sura facility [*Kotik and Ryabov*, 2011].

We restrict our discussion here to HAARP experiments that observed ICD generated ULF/ELF waves measured on the ground and simultaneously by DEMETER overflying at 670 km altitude and close to the HAARP Magnetic Zenith (MZ). In all cases the electrojet current, as determined by the magnetometer measurements and by using the strength of 2 kHz signals as proxy for the strength of electrojet [*Papadopoulos et al.*, 2011b], was absent. In all the examples shown here the ground signature is the magnetic signature of the generated signal while the satellite measures the electric field signal. Noise prevents magnetic field measurements at ULF/ELF frequencies in the noisy trough ionosphere above HAARP.

[31] A typical ICD experiment was performed on October 30, 2010 from 06:00:00–06:19:30 UT. During the experiment, HAARP transmitted at 2.8 MHz, O-mode, at peak power (3.6 MW), an amplitude modulated square waveform at 2.5 Hz, with the heater beam pointing along the magnetic zenith direction. The local VHF Riometer showed low absorption at ~ 0.2 dB at 30 MHz. The onsite fluxgate magnetometer showed flat HDZ traces with no fluctuation, indicating a very quiet ionosphere. The onsite digisonde showed foF2 at 1.45 MHz and F-peak at 260 km altitude with extremely weak E-layer. Figure 14 shows the wave spectrum measured simultaneously on the ground approximately 20 km away from the HAARP heater and by the

overflying DEMETER. Figure 14 (top left) is a projection of the DEMETER orbit moving with respect to the HAARP MZ. The red marking on the orbit represents the orbit part during which there was a strong signal at the injected frequency. The time duration was 20–25 s that corresponds to a distance of 100–150 km. The most important aspect of the measurement is the observed strong confinement of the ELF waves to the injection field line as expected by shear Alfvén waves and as seen in the simulation in Figure 4.

[32] This should be compared with Figure 15a that shows the electric field spectrum measured by DEMETER during a 0.1 Hz modulation along three color-coded parts of the trajectory. Notice that the 0.1 Hz signal was detected between 06:51:19 and 06:53:19 UT, approximately six times longer than the signal measured in the previous cases. In fact the low frequency and strong signal in this case allowed for the measurement of the waveform of the electric field shown in Figure 15b. We identify this wave with a magnetosonic wave that propagates isotropically, as seen in the simulation results of Figure 5.

[33] A most unexpected result revealed by the simulations is the distribution of the ELF magnetic amplitude on the ground signatures as a function of distance from the heater, shown in Figure 9. Previous experience with ELF and ULF waves generated by modulating the Polar Electrojet (PEJ) [Rietveld *et al.*, 1984, 1987, 1989; Papadopoulos *et al.*, 1990, 2005; Moore, 2007; Payne *et al.*, 2007] indicated that the wave amplitude had a maximum in the vicinity of the heater while monotonically decreasing with distance in a fashion consistent with guided wave propagation. However, as noted in Section 3.3, ICD driven waves have a minimum at the ground location defined by its interception with the magnetic field line that passes through the heated volume. This is seen clearly in the vertical magnetic field case (Figure 9a) where the magnetic field has a null at the transmitter location and a maximum approximately 200 km away. Figure 16 shows the results of a HAARP test conducted under daytime conditions during the period 17–25 August, 2009. The magnetic signals were measured simultaneously in Gakona and in Homer 300 km away. A number of frequencies between 12 Hz and 44 Hz were generated and simultaneously measured at the two sites. The signals are numbered from 1–40 and their frequency is color-coded. Signals 18–27 were generated by PEJ modulation while the remaining by ICD. It is clear that signals 18–27 are larger in Gakona than Homer consistent with previous PEJ observations. However, the situation is reversed for the remaining ICD signals many of which were detected only in Homer and not in Gakona. This, as explained previously and seen in the simulations, is a result of the two-step ELF generation by ICD. Namely the Hall current that acts as a secondary antenna that generates the ground signals occurs at the intersection of the magnetosonic wave with the Hall region. As a result the minimum occurs at the intersection of the magnetic field line with ground and the maximum at a distance that depends on the heating altitude and the geomagnetic latitude.

[34] We finally present some results indicative of far propagation of magnetosonic waves in the Alfvénic duct and measurements on the ground that indicate the presence of

skip distance such as seen in the simulations of Figure 9. Magnetometers were located in Gakona, Alaska, as well as in Lake Ozette, WA (2100 km), Makua Valley, Hawaii (4700 km) and Guam (7700 km) marked in Figure 17 (bottom right). The three diagrams in Figure 17 show magnetometer measurements taken during three different campaigns in 2009. It is important to mention that all the measurements shown in the figures correspond to ICD generation. The far sites did not record any signals 0.1–40 Hz range of our experiments during PEJ generation.

[35] A more comprehensive analysis of the far site results along with detailed modeling will be presented elsewhere. As an example we present here only the analysis and spectra measured by the ground ELF sites during the ICD experiment conducted May 6, 2009 between 08:00:15 and 08:20:15 UT, at a modulation frequency 3.8 Hz and detected by all the available ground sites in Figure 17. Figure 18 shows the ground magnetometer measurement at Gakona indicating that there was no electrojet over the site during the experiment time. This was also verified by the absence of 2 kHz signals when it was tested between 08:00:00 and 08:00:15. Figure 19 shows the ionosonde measurement indicating the absence of D/E regions and a strong F-layer with FoF2 close to 3.00 MHz. The HAARP heater operated at full power (3.6 MW), O-mode and frequency 3.25 MHz, consistent with under-dense heating. Figure 20 shows the ELF spectra measured at the four sites during the 20 minutes experiment time. In all cases there is a modest 3.8 Hz peak, and the S/N ratio is approximately 3 dB. The measured amplitudes vary between 30–40 fT.

[36] Our tentative conclusion of the results shown in Figure 17 is that the signals received in the far sites propagated laterally in the Alfvénic waveguide as magnetosonic waves generated by ICD. Their ground signatures were localized in regions where the magnetosonic wave reached the E-region after reflection from the top of the Alfvénic guide. We attribute the spottiness of the ground measurements in the fact that the skip distance in the Alfvénic guide depends on the ionospheric parameters that are highly dynamic and variable with latitude and time and to the value of the Hall conductivity at the E-region reflection points of the magnetosonic waves. We should also caution the reader that a comparison of the simulations with the far field measurements beyond a qualitative or notional level is not possible, since the simulations assumed a laterally homogeneous ionosphere and a highly unrealistic constant direction of the ambient magnetic field with latitude.

5. Conclusions

[37] We have here developed a cold plasma model for the propagation of ELF and ULF electromagnetic waves in the Earth's ionosphere, which we have used to study the dynamics of waves that are generated by the modulation of the electron pressure via external high-frequency heating of the F2 peak. Of particular interest is the penetration of the ULF waves through the ionospheric layer down to the free-space atmosphere and to the ground for different configurations of the geomagnetic field lines. At high altitudes, where ion-neutral and electron-neutral collisions are relatively rare,

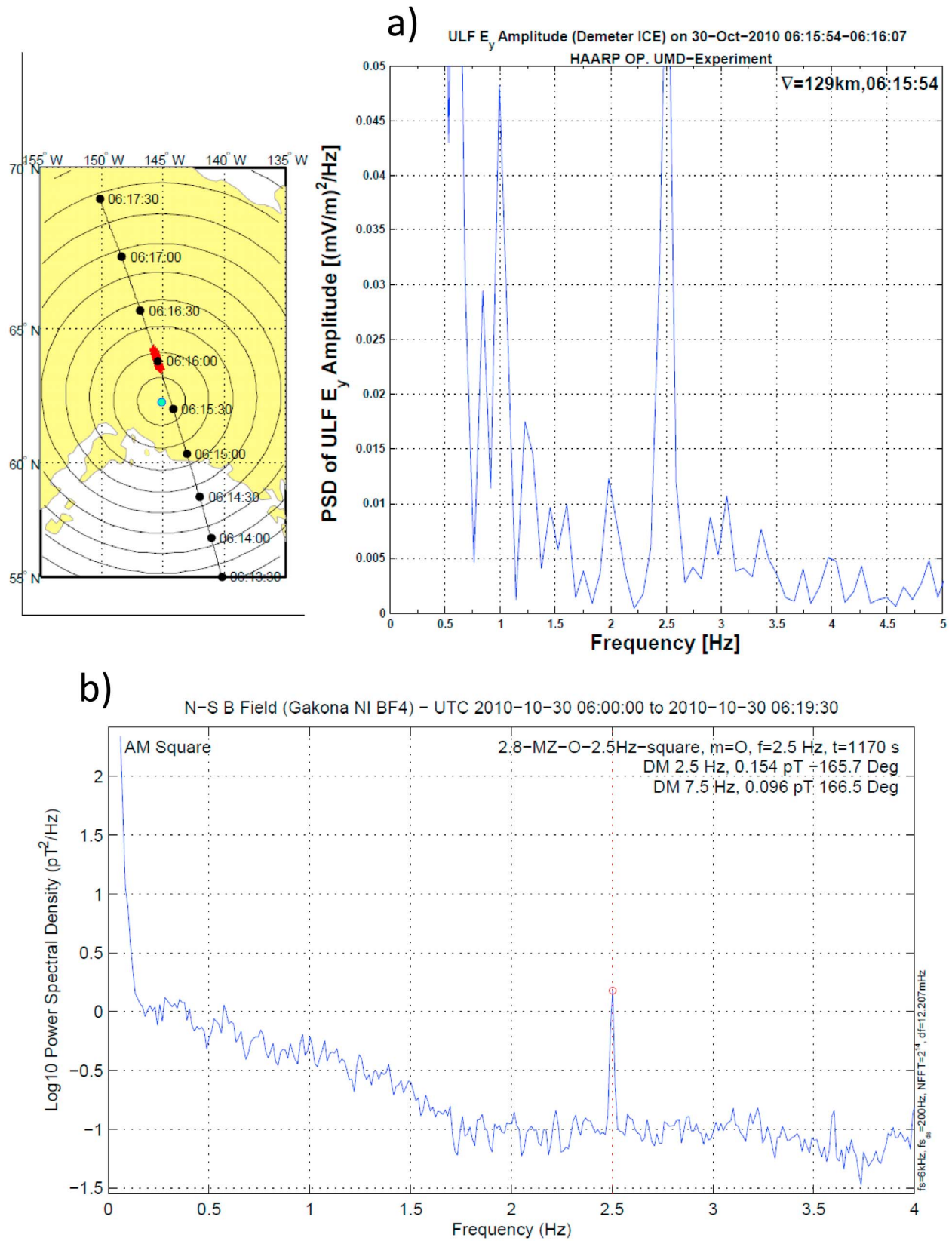


Figure 14. (a) Electric field spectrum measured by DEMETER during 2.5 Hz modulation of the HAARP heater. The heater operated at full power (3.6 MW), 2.8 MHz frequency and O-mode polarization. The top left diagram indicates the DEMETER location with respect to the HAARP MZ. (b) Magnetic field spectrum measured at Gakona simultaneously with DEMETER.

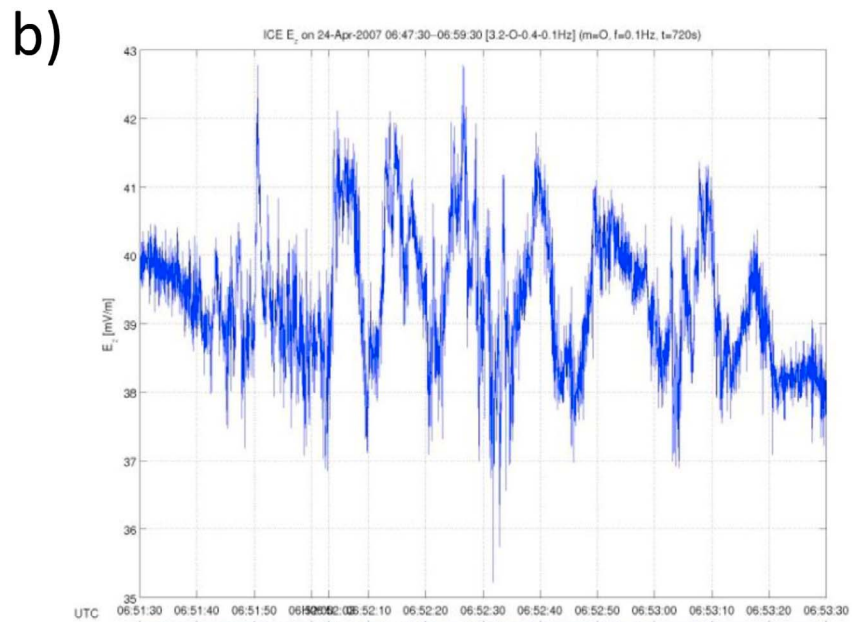
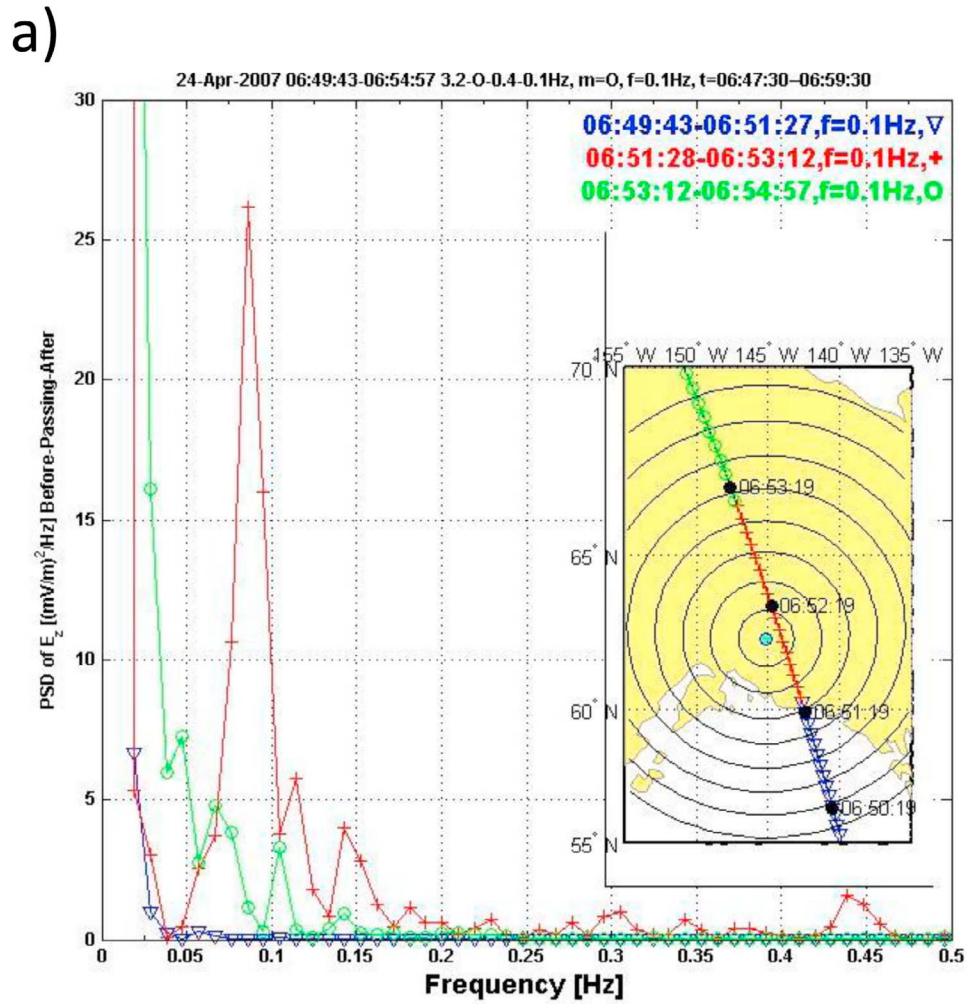


Figure 15

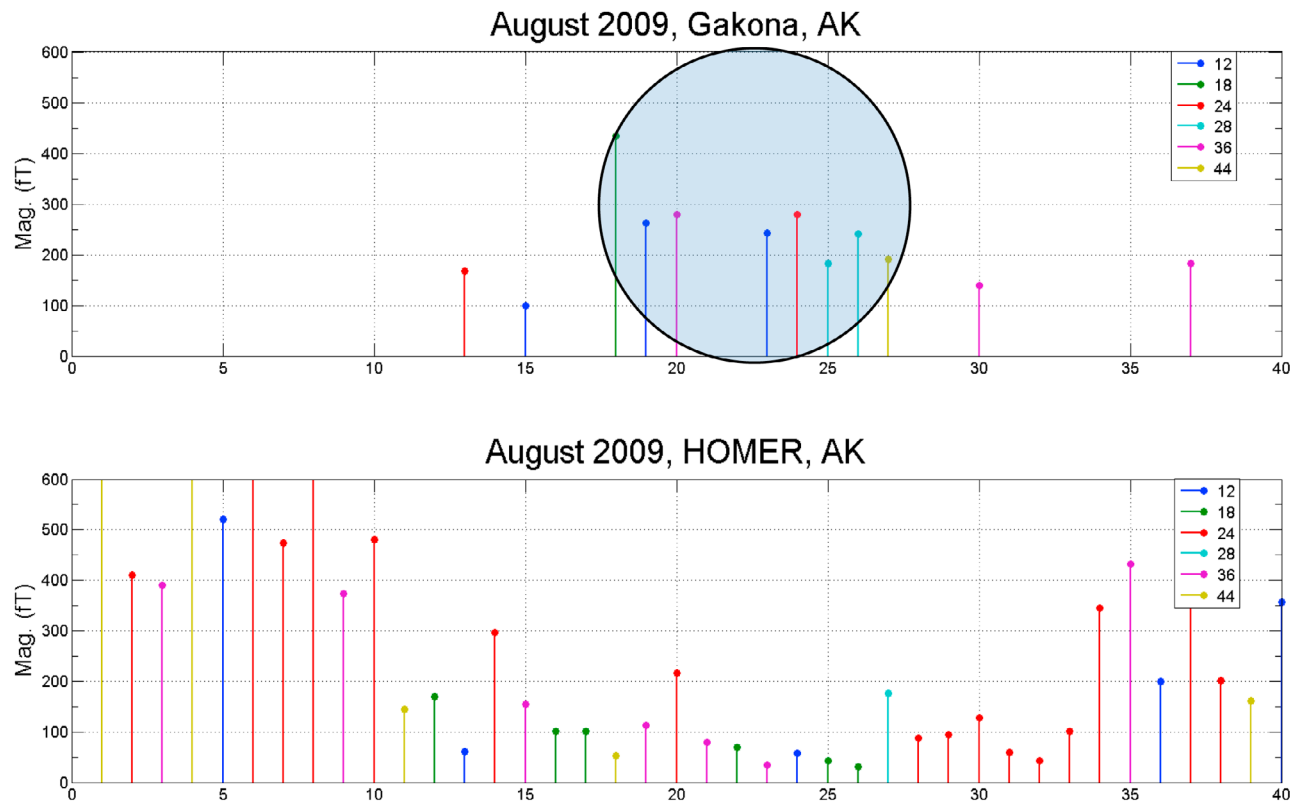


Figure 16. ELF wave amplitudes simultaneously measured at Gakona, AK, site of HAARP and Homer, AK, 330 km away for different frequencies 12–44 Hz (color coded). The different ELF signals are enumerated 1–40 (horizontal axis). The blue circle indicates ELF waves (signals 18–27) generated by PEJ current modulation, while the remaining by ICD. Contrary to the PEJ generated waves the amplitudes of the ICD waves were larger at the further site consistent with the simulation results shown in Figure 9a.

the dynamics is governed by the polarization current, which gives rise to the magnetosonic and shear Alfvén waves. When the ion-neutral collision frequency is larger than the wave frequency, but smaller than the ion cyclotron frequency, the ions and electrons experience $\mathbf{E} \times \mathbf{B}_0$ drift, and the ion current partially cancels the electron Hall current. This gives rise to a diffusive behavior of the plasma where the Pedersen conductivity dominates. In the Hall region below 120 km, the ions are collisionally glued to the neutrals while the electrons are mobile, which gives rise to weakly damped helicon wave dynamics governed by the Hall conductivity of the electrons. To understand the propagation of ELF and ULF waves through these layers down to the ground, we have performed simulations of the governing time-dependent equations for typical ionospheric parameters and analyzed the dispersive properties of the waves. We find that in the auroral region, where the geomagnetic field is

almost vertical, the right-hand circularly polarized shear Alfvén wave can connect smoothly to the helicon wave via a transition through the Pedersen layer where it loses about one order of magnitude wave energy (a factor of a few wave amplitude). A similar behavior is seen for oblique geomagnetic fields, typical for mid-latitude heating facilities, where shear Alfvén waves propagate along the geomagnetic field lines and are injected into the earth-ionosphere waveguide. For horizontal geomagnetic fields the dynamics is interesting in that current continuity demands that no large vertical currents can exist close to the plasma-free space boundary. The physics is here very similar to the equatorial electrojet, where the Cowling effect gives rise to intense horizontal currents perpendicular to the geomagnetic field. Our simulation has shown that modest amplitudes of the heating in the experiment can give rise to thin ELF current sheets in the E-region with dipole moments of about 10^7 Am, which may

Figure 15. (a) Electric field spectrum measured during overfly of HAARP when the heater was modulated at 0.1 Hz. The heater was operating at full power (3.6 MW), and O-mode, 3.2 MHz frequency. The insert indicates by color the DEMETER locations when the data shown were plotted. Notice that the 0.1 Hz frequency appears as dominant only during the DEMETER crossings near the MZ position while it disappears before and after. Ground data were too noisy at 0.1 Hz to resolve the 0.1 Hz line during the crossing. Notice that the detection time was close to 2 minutes, vs. only 20–30 seconds for the cases shown in Figure 14. (b) Waveform of the electric field measured by DEMETER during the part of the orbit marked by red, showing clear 10-second oscillations.

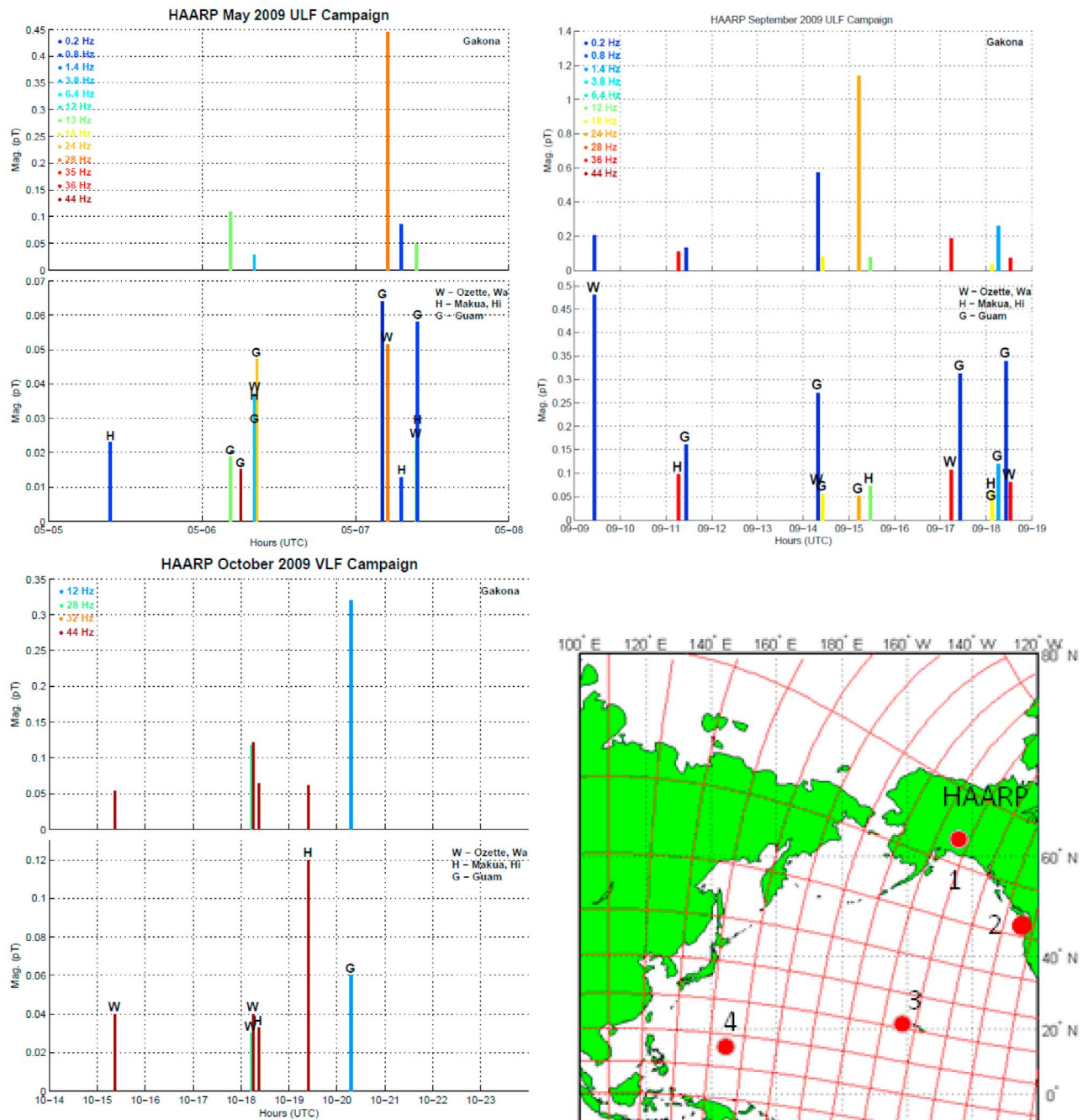


Figure 17. ICD generated ELF waves measured at 1. Gakona, Alaska, 2. Lake Ozette, WA (2100 km), 3. Makua Valley, Hawaii (4700 km) and 4. Guam (7700 km) during three campaigns conducted in 2009. Notice that in many cases the waves were detected only at the far sites and not in Gakona. A number of times the waves were measured at two or three sites. In only one case waves at 3.8 Hz with amplitude 30 fT were detected in all four sites (May 6, 2009, 08:00:15 UT to 08:20:15 UT). We attribute the unpredictable detection to the fact that the skip distance seen in the simulations of Figure 9 depends critically in the ionospheric conditions and to the noise at the detection site.

work as an antenna to inject electromagnetic waves into the earth-ionosphere waveguide. Some features of the modeling results are relevant for recent measurements of ICD generated ULF/ELF waves at HAARP, including a skip distance, where the ICD generated signal amplitude at the ground has a

minimum near the heater, in contrast to PEJ generated signals. Some far field observations are also consistent with ICD generated magnetosonic waves guided in the ionospheric waveguide, not observed for PEJ generated waves. These

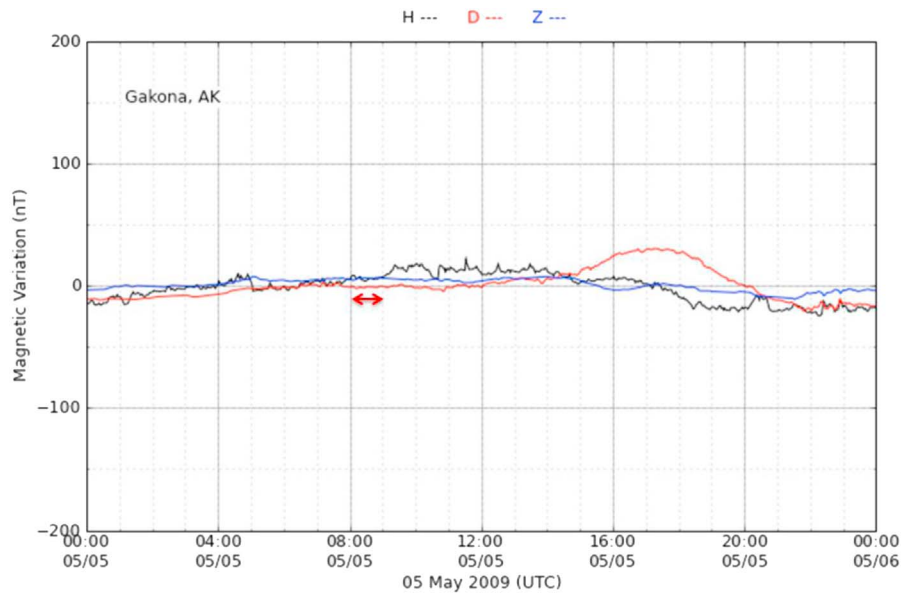


Figure 18. Gakona magnetometer measurement indicating the absence of the electrojet during the testing period (marked by red arrow).

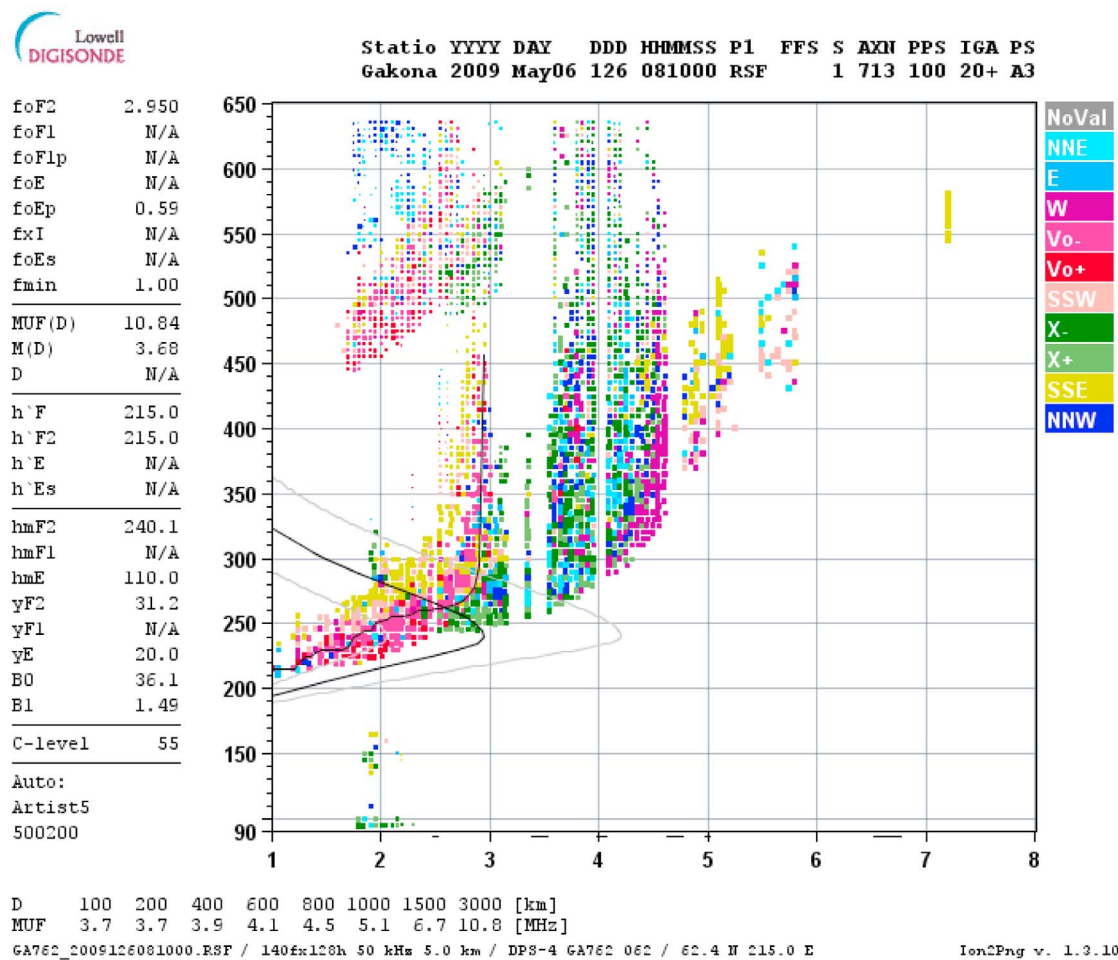


Figure 19. Gakona ionosonde measurement showing very weak D/E layers and a well-developed F-layer with FoF2 close to 3 MHz.

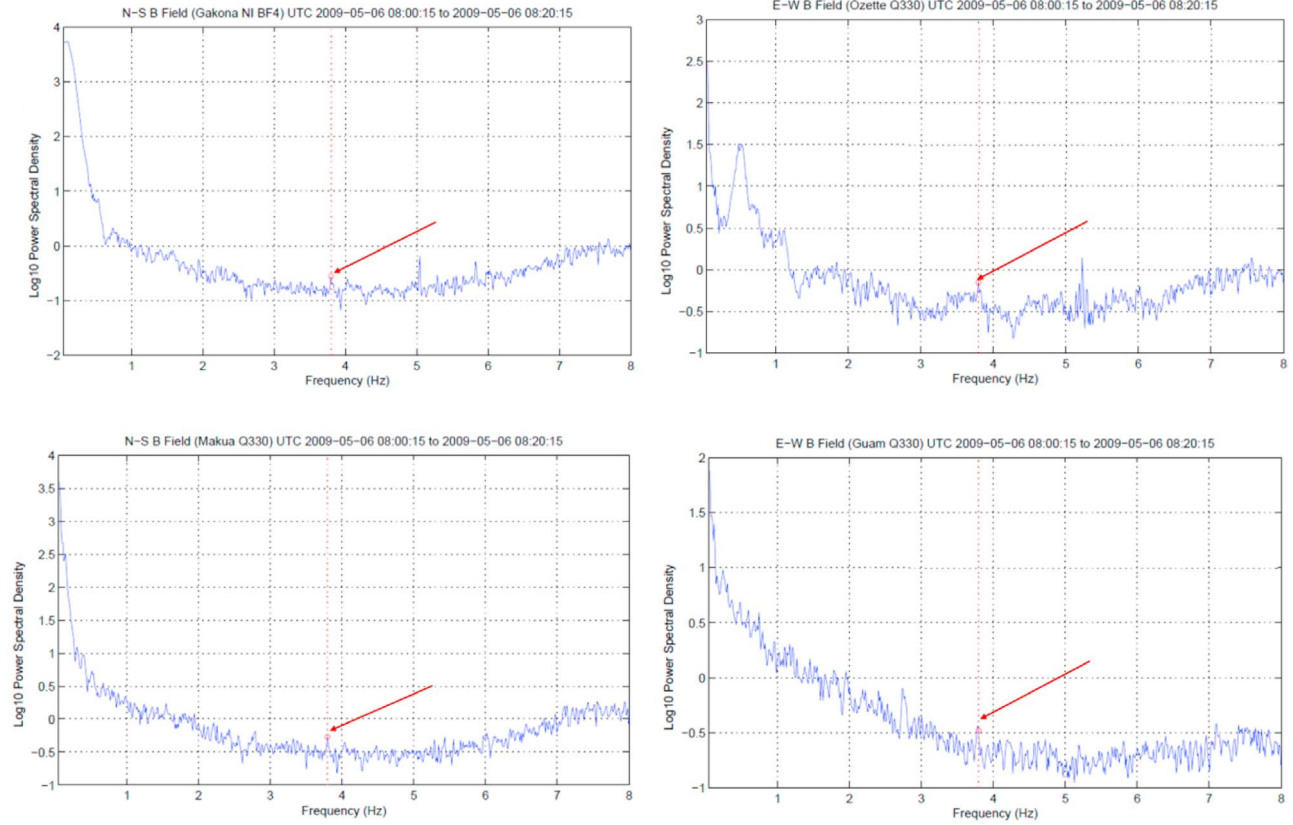


Figure 20. ELF spectra measured at the four sites shown in Figure 17 taken during the 20-minute transmission of 3.8 Hz modulated HF waves by the HAARP heater. The amplitude of the detected signal (marked by red arrows) was between 30–40 fT while the signal-to-noise ratio was close to 3 dB.

issues along with injection of ICD generated waves in the radiation belts will be discussed in a future publication.

Appendix A: Derivation of the Governing Equations Using Dielectric and Conductivity Tensors

[38] We here derive a cold plasma model for ELF and ULF wave propagation in the ionosphere, describing the interaction between the magnetic and electric fields in terms of dielectric and conductivity tensors. In order to reduce the analytic work, it is convenient to introduce matrix formalism and organize the vectors as column vectors to describe the electron and ion dynamics. By denoting

$$\frac{\mathbf{v}_e \times \mathbf{B}_0}{B_0} + \frac{m_e v_{en}}{e B_0} \mathbf{v}_e \equiv \overline{\overline{\mathbf{R}}}_e \mathbf{v}_e \quad (\text{A1})$$

and

$$\frac{\mathbf{v}_i \times \mathbf{B}_0}{B_0} - \frac{m_i v_{in}}{e B_0} \mathbf{v}_i \equiv \overline{\overline{\mathbf{R}}}_i \mathbf{v}_i, \quad (\text{A2})$$

where $\overline{\overline{\mathbf{R}}}_e$ and $\overline{\overline{\mathbf{R}}}_i$ are tensors/matrices operating on the vectors, the electron and ion momentum equations (3) and (4) can be written

$$\mathbf{E} = -B_0 \overline{\overline{\mathbf{R}}}_e \mathbf{v}_e - \frac{\nabla P_e}{en_0} \quad (\text{A3})$$

and

$$\frac{\partial \mathbf{v}_i}{\partial t} = \frac{e}{m_i} (\mathbf{E} + B_0 \overline{\overline{\mathbf{R}}}_i \mathbf{v}_i), \quad (\text{A4})$$

respectively. From equation (A3) we have, for example, $\mathbf{v}_e = -\overline{\overline{\mathbf{R}}}_e^{-1} [\mathbf{E} + \nabla P_e / (en_0)] / B_0$, where $\overline{\overline{\mathbf{R}}}_e^{-1}$ is the inverse of the tensor/matrix $\overline{\overline{\mathbf{R}}}_e$, given in equation (A10) below. An evolution equation for the electric field can be found by taking the time derivative of equation (A3) and expressing the right-hand side in terms of \mathbf{E} and \mathbf{B} . The result is

$$\frac{\partial \mathbf{E}}{\partial t} = \frac{e}{m_i} \left[B_0 (\overline{\overline{\mathbf{R}}}_i - \overline{\overline{\mathbf{R}}}_e) \mathbf{E} - \frac{B_0^2 \overline{\overline{\mathbf{R}}}_e \overline{\overline{\mathbf{R}}}_i (\nabla \times \mathbf{B})}{\mu_0 en_0} \right] - \frac{B_0}{\mu_0 en_0} \overline{\overline{\mathbf{R}}}_e [\nabla \times (\nabla \times \mathbf{E})] - \frac{1}{en_0} \nabla \frac{\partial P_e}{\partial t} + \frac{e B_0}{m_i} \overline{\overline{\mathbf{R}}}_i \frac{\nabla P_e}{en_0} \quad (\text{A5})$$

In deriving equation (A5), we have used that $\overline{\overline{\mathbf{R}}}_i$ and $\overline{\overline{\mathbf{R}}}_e$ commute, i.e. $\overline{\overline{\mathbf{R}}}_i \overline{\overline{\mathbf{R}}}_e = \overline{\overline{\mathbf{R}}}_e \overline{\overline{\mathbf{R}}}_i$. Equation (A5) can be written in the form

$$\frac{\partial \mathbf{E}}{\partial t} = \overline{\overline{\mathbf{E}}}^{-1} \left(-\overline{\overline{\mathbf{E}}} \mathbf{E} + \frac{\nabla \times \mathbf{B}}{\mu_0} \right) - \frac{\overline{\overline{\mathbf{R}}}_e [\nabla \times (\nabla \times \mathbf{E})]}{\mu_0 \tilde{\sigma}} - \frac{1}{en_0} \nabla \frac{\partial P_e}{\partial t} + \omega_{ci} \overline{\overline{\mathbf{R}}}_i \frac{\nabla P_e}{en_0}, \quad (\text{A6})$$

where $\bar{\bar{\epsilon}} = -(\epsilon_0 c^2 / v_A^2) (\bar{\bar{\mathbf{R}}}_e \bar{\bar{\mathbf{R}}}_i)^{-1}$ is the effective dielectric tensor, $v_A = c \omega_{ci} / \omega_{pi}$ is the Alfvén speed, $\bar{\bar{\sigma}} = \tilde{\sigma} (\bar{\bar{\mathbf{R}}}_e^{-1} - \bar{\bar{\mathbf{R}}}_i^{-1})$ is the conductivity tensor, and we denoted $\tilde{\sigma} = \epsilon_0 \omega_{pe}^2 / \omega_{ce}$. Using the definitions (A1) and (A2) of $\bar{\bar{\mathbf{R}}}_e$ and $\bar{\bar{\mathbf{R}}}_i$, we find that $\bar{\bar{\epsilon}}^{-1} \bar{\bar{\sigma}} \mathbf{E} = -\omega_{ci} (\bar{\bar{\mathbf{R}}}_i - \bar{\bar{\mathbf{R}}}_e) \mathbf{E} = \omega_{ci} (\Gamma_{in} + \Gamma_{en}) \mathbf{E}$, where we have denoted $\Gamma_{en} = v_{en} / \omega_{ce}$ and $\Gamma_{in} = v_{in} / \omega_{ci}$. Hence, equation (A6) can be written

$$\frac{\partial \mathbf{E}}{\partial t} = -\omega_{ci} (\Gamma_{in} + \Gamma_{en}) \mathbf{E} + \frac{\bar{\bar{\epsilon}}^{-1} \nabla \times \mathbf{B}}{\mu_0} - \frac{\bar{\bar{\mathbf{R}}}_e [\nabla \times (\nabla \times \mathbf{E})]}{\mu_0 \tilde{\sigma}} - \frac{1}{en_0} \nabla \frac{\partial P_e}{\partial t} + \omega_{ci} \mathbf{R}_i \frac{\nabla P_e}{en_0} \quad (\text{A7})$$

The last step is to introduce the scalar and vector potentials ϕ and \mathbf{A} via $\mathbf{B} = \nabla \times \mathbf{A}$ and $\mathbf{E} = -\nabla \phi - \partial \mathbf{A} / \partial t$ using the gauge $\phi = 0$. Faraday's law (1) is then fulfilled trivially and we obtain the system (5)–(6).

[39] It is instructive to discuss some limiting cases of the governing equations without the driving terms proportional to P_e . We note that the left-hand side of equation (A6) is associated with the polarization current, i.e. $\mathbf{j}_p = \bar{\bar{\epsilon}} \partial \mathbf{E} / \partial t$. In the collisionless limit $\omega_{ci} (\Gamma_{in} + \Gamma_{en}) \ll |\partial / \partial t|$, the polarization current dominates the physics and we have shear Alfvén and magnetosonic waves. In the limit $\Gamma_e = \Gamma_i = 0$, equation (A7), using the expressions of $\bar{\bar{\epsilon}}^{-1}$, $\bar{\bar{\mathbf{R}}}_e$ and $\bar{\bar{\mathbf{R}}}_i$, reduces to the collisionless Hall-MHD equation

$$\frac{\partial \mathbf{E}}{\partial t} = -\frac{v_A^2}{B_0^2} [(\nabla \times \mathbf{B}) \times \mathbf{B}_0] \times \mathbf{B}_0 - \frac{c^2 \omega_{ce}}{\omega_{pe}^2 B_0^2} [\nabla \times (\nabla \times \mathbf{E})] \times \mathbf{B}_0. \quad (\text{A8})$$

[40] In the frequency range much below the ion cyclotron frequency, equation (A8) reduces further to the ideal MHD equation

$$\frac{\partial \mathbf{E}}{\partial t} = -\frac{v_A^2}{B_0^2} [(\nabla \times \mathbf{B}) \times \mathbf{B}_0] \times \mathbf{B}_0, \quad (\text{A9})$$

which, together with equation (1), supports the shear Alfvén and magnetosonic wave modes. In the opposite limit, when $\omega_{ci} (\Gamma_{in} + \Gamma_{en}) \gg |\partial / \partial t|$, the ion inertial effects (and thus the polarization current) can be neglected, and the current is given by the plasma conductivity as $\mathbf{j} = \bar{\bar{\sigma}} \mathbf{E}$. We then have from equation (A6) the quasi-steady state limit (omitting the externally modulated electron pressure) $-\bar{\bar{\sigma}} \mathbf{E} + \nabla \times \mathbf{B} / \mu_0 = 0$, which, coupled with equation (1), supports helicon/whistler wave dynamics in the frequency range below the ion cyclotron frequency when $\sigma_H \gg \sigma_P$, and diffusive behavior for $\sigma_P \gg \sigma_H$.

[41] There are also time-independent and non-propagating, damped solutions of the system (5) and (6). We see that $\mathbf{E} = 0$ and $\mathbf{A} = \nabla U$, where $U(\mathbf{r})$ depends only on space, is a time-independent solution (conserved quantity) of equations (5) and (6). For the case $\Gamma_{in} + \Gamma_{en} = \text{constant}$, we have with $\mathbf{E} = -\nabla \phi$ into (5) and (6), $\partial \mathbf{A} / \partial t = -\mathbf{E}$ and $\partial \mathbf{E} / \partial t = -\omega_{ci} (\Gamma_{in} + \Gamma_{en}) \mathbf{E}$, which have solutions proportional to $\exp[-\omega_{ci} (\Gamma_{in} + \Gamma_{en}) t]$ that decay in time but do not propagate in space. This mode does not involve the excitation of magnetic fields since $\nabla \times \mathbf{E} = -\nabla \times \nabla \phi = 0$ in

equation (1). In our model, since the term proportional to $\nabla \partial P_e / \partial t$ in the right-hand side of equation (6) is the gradient of a scalar, it primarily excites the non-propagating modes and not the electromagnetic modes.

[42] We next give the expressions of the dielectric and conductivity tensors, and their inverses, in matrix form. For the case where \mathbf{B}_0 is directed along the x -axis, we have

$$\bar{\bar{\mathbf{R}}}_e = \begin{bmatrix} \Gamma_{en} & 0 & 0 \\ 0 & \Gamma_{en} & 1 \\ 0 & -1 & \Gamma_{en} \end{bmatrix}, \quad \bar{\bar{\mathbf{R}}}_e^{-1} = \begin{bmatrix} \Gamma_{en}^{-1} & 0 & 0 \\ 0 & \frac{\Gamma_{en}}{1 + \Gamma_{en}^2} & \frac{-1}{1 + \Gamma_{en}^2} \\ 0 & \frac{1}{1 + \Gamma_{en}^2} & \frac{\Gamma_{en}}{1 + \Gamma_{en}^2} \end{bmatrix} \quad (\text{A10})$$

and

$$\bar{\bar{\mathbf{R}}}_i = \begin{bmatrix} -\Gamma_{in} & 0 & 0 \\ 0 & -\Gamma_{in} & 1 \\ 0 & -1 & -\Gamma_{in} \end{bmatrix}, \quad \bar{\bar{\mathbf{R}}}_i^{-1} = \begin{bmatrix} -\Gamma_{in}^{-1} & 0 & 0 \\ 0 & \frac{-\Gamma_{in}}{1 + \Gamma_{in}^2} & \frac{-1}{1 + \Gamma_{in}^2} \\ 0 & \frac{1}{1 + \Gamma_{in}^2} & \frac{-\Gamma_{in}}{1 + \Gamma_{in}^2} \end{bmatrix}. \quad (\text{A11})$$

[43] The conductivity tensor is

$$\bar{\bar{\sigma}} = \tilde{\sigma} (\bar{\bar{\mathbf{R}}}_e^{-1} - \bar{\bar{\mathbf{R}}}_i^{-1}) = \begin{bmatrix} \sigma_{\parallel} & 0 & 0 \\ 0 & \sigma_P & -\sigma_H \\ 0 & \sigma_H & \sigma_P \end{bmatrix}, \quad (\text{A12})$$

where the parallel, Pedersen, and Hall conductivity, respectively, are given by $\sigma_{\parallel} = \tilde{\sigma} (\Gamma_{en}^{-1} + \Gamma_{in}^{-1})$, $\sigma_P = \tilde{\sigma} [\Gamma_{en} / (1 + \Gamma_{en}^2) + \Gamma_{in} / (1 + \Gamma_{in}^2)]$, and $\sigma_H = \tilde{\sigma} [1 / (1 + \Gamma_{en}^2) - 1 / (1 + \Gamma_{in}^2)]$. The dielectric tensor $\bar{\bar{\epsilon}}$ is proportional to the conductivity tensor $\bar{\bar{\sigma}}$, as $\bar{\bar{\epsilon}} = \bar{\bar{\sigma}} / [\omega_{ci} (\Gamma_{in} + \Gamma_{en})]$, and the inverse of the dielectric tensor is given by

$$\bar{\bar{\epsilon}}^{-1} = \epsilon_0^{-1} \frac{v_A^2}{c^2} \begin{bmatrix} \Gamma_{in} \Gamma_{en} & 0 & 0 \\ 0 & 1 + \Gamma_{in} \Gamma_{en} & \Gamma_{in} - \Gamma_{en} \\ 0 & \Gamma_{en} - \Gamma_{in} & 1 + \Gamma_{in} \Gamma_{en} \end{bmatrix}. \quad (\text{A13})$$

[44] The general case of oblique and \mathbf{r} -dependent geomagnetic fields are obtained by multiplying the above matrices by rotation matrices, as $\bar{\bar{\mathbf{A}}} = \bar{\bar{\mathbf{S}}} \bar{\bar{\mathbf{A}}}_x \bar{\bar{\mathbf{S}}}^{-1}$, where $\bar{\bar{\mathbf{A}}}_x$ represents any of the matrices for the case when the geomagnetic field is parallel to the x -axis. The rotation matrix and its inverse are given by

$$\bar{\bar{\mathbf{S}}} = \begin{bmatrix} \sin(\theta) & 0 & -\cos(\theta) \\ 0 & 1 & 0 \\ \cos(\theta) & 0 & \sin(\theta) \end{bmatrix}, \quad \bar{\bar{\mathbf{S}}}^{-1} = \begin{bmatrix} \sin(\theta) & 0 & \cos(\theta) \\ 0 & 1 & 0 \\ -\cos(\theta) & 0 & \sin(\theta) \end{bmatrix}, \quad (\text{A14})$$

where θ is the angle between the vertical z -axis and the magnetic field lines, defined via the relations $\sin(\theta) = B_{0x} / B_0$ and $\cos(\theta) = B_{0z} / B_0$, and which may vary in space,

$\theta = \theta(\mathbf{r})$. The matrices $\overline{\overline{\mathbf{R}}}_e$, $\overline{\overline{\mathbf{R}}}_i$, $\overline{\overline{\mathbf{E}}}$, and $\overline{\overline{\mathbf{O}}}$, and their inverses, are all of the general form

$$\overline{\overline{\mathbf{A}}}_x = \begin{bmatrix} a_{\parallel} & 0 & 0 \\ 0 & a_P & a_H \\ 0 & -a_H & a_P \end{bmatrix} \quad (\text{A15})$$

for $\theta = 90^\circ$, from which we obtain the general case of arbitrary θ as

$$\overline{\overline{\mathbf{A}}} = \begin{bmatrix} a_{11} & a_{12} & a_{13} \\ -a_{12} & a_{22} & a_{23} \\ a_{13} & -a_{23} & a_{33} \end{bmatrix} \quad (\text{A16})$$

where $a_{11} = a_{\parallel} \sin^2(\theta) + a_P \cos^2(\theta)$, $a_{12} = a_H \cos(\theta)$, $a_{13} = (a_{\parallel} - a_P) \cos(\theta) \sin(\theta)$, $a_{22} = a_P$, $a_{23} = a_H \sin(\theta)$, and $a_{33} = a_{\parallel} \cos^2(\theta) + a_P \sin^2(\theta)$.

Appendix B: Boundary Conditions and Free Space Electromagnetic Fields

[45] In our model, free space is characterized by infinite speed of light, while the ground is perfectly conducting. At the plasma-free space boundary, the x - and y -components of the electric field and vector potential, as well as their normal derivatives, are continuous over the boundary, while at the ground the x - and y -components of the electric field and vector potential are zero. Hence, the boundary conditions and free space fields are analogous for \mathbf{E} and \mathbf{A} , and it is sufficient to discuss the electric field.

[46] The free space electric field \mathbf{E}_{free} is governed by $\nabla^2 \mathbf{E}_{free} = 0$. Fourier transforming in the x -direction by assuming that \mathbf{E}_{free} is proportional to $\exp(ik_x x)$, gives

$$\frac{\partial^2 \mathbf{E}_{free}}{\partial z^2} - k_x^2 \mathbf{E}_{free} = 0, \quad (\text{B1})$$

with the general solution

$$\mathbf{E}_{free} = \mathbf{C}_1 \exp(|k_x|z) + \mathbf{C}_2 \exp(-|k_x|z), \quad (\text{B2})$$

where \mathbf{C}_1 and \mathbf{C}_2 are vector-valued integration constants with components along the x - and y -directions. Since E_x and E_y and their normal derivatives are continuous at $z = z_0$, we have for the x - and y -components of the electric field,

$$\begin{aligned} \mathbf{E}_{plasma}(z = z_0) &= \mathbf{E}_{free}(z = z_0) \\ &= \mathbf{C}_1 \exp(|k_x|z_0) + \mathbf{C}_2 \exp(-|k_x|z_0) \end{aligned} \quad (\text{B3})$$

and

$$\begin{aligned} \frac{\partial \mathbf{E}_{plasma}}{\partial z}(z = z_0) &= \frac{\partial \mathbf{E}_{free}}{\partial z}(z = z_0) \\ &= |k_x|[\mathbf{C}_1 \exp(|k_x|z_0) - \mathbf{C}_2 \exp(-|k_x|z_0)]. \end{aligned} \quad (\text{B4})$$

[47] At the perfectly conducting ground we have $\mathbf{E}_{free}(z = 0) = 0$, hence $\mathbf{C}_2 = -\mathbf{C}_1$, and from equation (B3) we obtain (dropping the subscripts ‘‘plasma’’ and ‘‘free’’ on \mathbf{E})

$$\mathbf{C}_1 = -\mathbf{C}_2 = \frac{\mathbf{E}(z = z_0)}{\exp(|k_x|z_0) - \exp(-|k_x|z_0)}. \quad (\text{B5})$$

[48] Eliminating \mathbf{C}_1 and \mathbf{C}_2 from equation (B4), we obtain the plasma-free space boundary condition at $z = z_0$,

$$\frac{\partial \mathbf{E}}{\partial z} = \alpha(|k_x|)\mathbf{E}, \quad (\text{B6})$$

where

$$\alpha(|k_x|) = \frac{\exp(|k_x|z_0) + \exp(-|k_x|z_0)}{\exp(|k_x|z_0) - \exp(-|k_x|z_0)} |k_x| \quad (\text{B7})$$

for $|k_x| > 0$, and $\alpha = 1/z_0$ for $k_x = 0$. The inverse Fourier transform of \mathbf{E} with respect to k_x gives the boundary condition in real space.

[49] The free space electric field in the region $0 < z < z_0$ is obtained from (B2) by using (B5) as

$$\mathbf{E}_{free} = \frac{\exp(|k_x|z) - \exp(-|k_x|z)}{\exp(|k_x|z_0) - \exp(-|k_x|z_0)} \mathbf{E}(z = z_0). \quad (\text{B8})$$

[50] The same boundary conditions are used for the x - and y -components of the vector potential \mathbf{A} , so that

$$\frac{\partial \mathbf{A}}{\partial z} = \alpha(|k_x|)\mathbf{A}, \quad (\text{B9})$$

at $z = z_0$, and

$$\mathbf{A}_{free} = \frac{\exp(|k_x|z) - \exp(-|k_x|z)}{\exp(|k_x|z_0) - \exp(-|k_x|z_0)} \mathbf{A}(z = z_0). \quad (\text{B10})$$

[51] The z -component of the vector potential is obtained from the assumption that $B_y = \partial A_x / \partial z - \partial A_z / \partial x = 0$ at the boundary, or with $\partial / \partial x = ik_x$,

$$A_z = \frac{1}{ik_x} \frac{\partial A_x}{\partial z} \quad (\text{B11})$$

at $z = z_0$. Similarly, since \mathbf{A} and \mathbf{E} are related by a time derivative, we have

$$E_z = \frac{1}{ik_x} \frac{\partial E_x}{\partial z} \quad (\text{B12})$$

at $z = z_0$. The vertical components of the free space vector potential and electric field are

$$A_{z,free} = \frac{1}{ik_x} \frac{\partial A_x}{\partial z} = \frac{|k_x|}{ik_x} \frac{\exp(|k_x|z) + \exp(-|k_x|z)}{\exp(|k_x|z_0) - \exp(-|k_x|z_0)} A_x(z = z_0) \quad (\text{B13})$$

and

$$E_{z,free} = \frac{1}{ik_x} \frac{\partial E_x}{\partial z} = \frac{|k_x|}{ik_x} \frac{\exp(|k_x|z) + \exp(-|k_x|z)}{\exp(|k_x|z_0) - \exp(-|k_x|z_0)} E_x(z = z_0) \quad (\text{B14})$$

respectively, for $0 < z < z_0$. The free space magnetic field is obtained as $\mathbf{B}_{free} = \nabla \times \mathbf{A}_{free}$, while the current in free space is zero, $\mathbf{j}_{free} = 0$.

[52] The numerical approximation of the boundary conditions (B6) and (B9) are done with one-sided difference

approximations $(\mathbf{E}_1 - \mathbf{E}_0)/\Delta z = \alpha \mathbf{E}_0$ and $(\mathbf{A}_1 - \mathbf{A}_0)/\Delta z = \alpha \mathbf{A}_0$, where the subscript 0 denotes the unknown value at the boundary point and subscript 1 the known value at the neighboring point inside the computational domain. Solving for \mathbf{E}_0 and \mathbf{A}_0 , we obtain the numerical boundary conditions

$$\mathbf{E}_0 = \frac{\mathbf{E}_1}{1 + \alpha \Delta z}, \quad (\text{B15})$$

and

$$\mathbf{A}_0 = \frac{\mathbf{A}_1}{1 + \alpha \Delta z}, \quad (\text{B16})$$

respectively. The boundary conditions (B11) and (B12) are approximated as

$$A_{z,0} = \frac{1}{ik_x} \frac{A_{x,1} - A_{x,0}}{\Delta z} \quad (\text{B17})$$

and

$$E_{z,0} = \frac{1}{ik_x} \frac{E_{x,1} - E_{x,0}}{\Delta z}, \quad (\text{B18})$$

where $E_{x,0}$ and $A_{x,0}$ are obtained from equations (B15) and (B17), respectively. At the top boundary at $z = 1020$ km, we use first-order outflow boundary conditions $\partial \mathbf{A} / \partial t + v_A \partial \mathbf{A} / \partial z = 0$ and $\partial \mathbf{E} / \partial t + v_A \partial \mathbf{E} / \partial z = 0$ for \mathbf{E} and \mathbf{A} , where v_A is the Alfvén speed at the top boundary, and where the z derivatives are calculated with one-sided difference approximations.

[53] **Acknowledgments.** This work was partially supported by ONR MURI N00014-07-1-0789 and DARPA-DSO HR0011-09C-0099 contract to BAE-Systems. The authors are grateful to Nail Gumerov, Gennady Milikh, Xi Shao, Aram Vartanyan and A. S. Sharma at the University of Maryland and to T. Wallace, John Labenski and I. Doxas at BAE Systems - AT for useful discussions. B. E. acknowledges the hospitality of University of Maryland, as well as partial support by the DFG FOR1048 (Bonn, Germany).

[54] Robert Lysak thanks Jean-Andre Sauvaud and another reviewer for their assistance in evaluating this paper.

References

- Barr, R. (1998), The generation of ELF and VLF radio waves in the ionosphere using powerful HF transmitters, *Adv. Space Res.*, 21(5), 677–687, doi:10.1016/S0273-1177(97)01003-X.
- Berthelier, J.-J., M. Malingre, R. Pfaff, E. Seran, R. Pottelette, J. Jasperse, J.-P. Lebreton, and M. Parrot (2008), Lightning-induced plasma turbulence and ion heating in equatorial ionospheric depletions, *Nat. Geosci.*, 1, 101–105, doi:10.1038/ngeo109.
- Berthold, W. K., A. K. Harris, and H. J. Hope (1960), World-wide effects of hydromagnetic waves due to Argus, *J. Geophys. Res.*, 65(8), 2233–2239, doi:10.1029/JZ065i008p02233.
- Dessler, A. J. (1958), The propagation velocity of world-wide sudden commencements of magnetic storms, *J. Geophys. Res.*, 63(2), 405–408, doi:10.1029/JZ063i002p00405.
- Eliasson, B., and K. Papadopoulos (2009), Penetration of ELF currents and magnetic fields into the Earth's equatorial ionosphere, *J. Geophys. Res.*, 114, A10301, doi:10.1029/2009JA014213.
- Forbes, J. M. (1981), The equatorial electrojet, *Rev. Geophys.*, 19, 469–504, doi:10.1029/RG019i003p00469.
- Forbes, J. M., and R. S. Lindzen (1976), Atmospheric solar tides and their electrodynamic effects—II. The equatorial electrojet, *J. Atmos. Terr. Phys.*, 38(9–10), 911–920, doi:10.1016/0021-9169(76)90074-X.
- Ganguly, S., W. Gordon, and K. Papadopoulos (1986), Active nonlinear ultralow-frequency generation in the ionosphere, *Phys. Rev. Lett.*, 57, 641–644, doi:10.1103/PhysRevLett.57.641.
- Greifinger, C., and P. S. Greifinger (1968), Theory of hydromagnetic propagation in the ionospheric waveguide, *J. Geophys. Res.*, 73(23), 7473–7490, doi:10.1029/JA073i023p07473.
- Greifinger, C., and P. Greifinger (1973), Wave guide propagation of micropulsations out of the plane of the geomagnetic meridian, *J. Geophys. Res.*, 78(22), 4611–4618, doi:10.1029/JA078i022p04611.
- Greifinger, C., and P. Greifinger (1976), Transient ULF electric and magnetic fields following a lightning discharge, *J. Geophys. Res.*, 81(13), 2237–2247, doi:10.1029/JA081i013p02237.
- Hayakawa, M., S. Pulintets, M. Parrot, and O. A. Molchanov (2006), Recent progress in seismo electromagnetics and related phenomena, *Phys. Chem. Earth, Parts A/B/C*, 31(4–9), 129–131.
- Kotik, D., and A. Ryabov (2011), New results of experiments on generation ULF/VLF waves with SURA facility, Abstract SA42A-06 presented at 2011 Fall Meeting, AGU, San Francisco, Calif.
- Lysak, R. L. (1997), Propagation of Alfvén waves through the ionosphere, *Phys. Chem. Earth*, 22, 757–766, doi:10.1016/S0079-1946(97)00208-5.
- Lysak, R. L. (1999), Propagation of Alfvén waves through the ionosphere: Dependence on ionospheric parameters, *J. Geophys. Res.*, 104, 10,017–10,030, doi:10.1029/1999JA900024.
- Lysak, R. L. (2004), Magnetosphere-ionosphere coupling by Alfvén waves at midlatitudes, *J. Geophys. Res.*, 109, A07201, doi:10.1029/2004JA010454.
- Lysak, R. L., and Y. Song (2001), A three-dimensional model of the propagation of Alfvén waves through the auroral ionosphere: First results, *Adv. Space Res.*, 28(5), 813–822, doi:10.1016/S0273-1177(01)00508-7.
- Milikh, G. M., K. Papadopoulos, and C. L. Chang (1995), On the physics of high altitude lightning, *Geophys. Res. Lett.*, 22(2), 85–88, doi:10.1029/94GL02733.
- Moore, R. C. (2007), ELF/VLF wave generation by modulated heating of the auroral electrojet, PhD thesis, Stanford Univ., Stanford, Calif.
- Papadopoulos, K. (2009), Ionospheric current drive at low frequencies, *Eos Trans. AGU*, 90(52), Fall Meet. Suppl., Abstract SA11B-01.
- Papadopoulos, K., C. L. Chang, P. Vitello, and A. Drobot (1990), On the efficiency of ionospheric ELF generation, *Radio Sci.*, 25(6), 1311–1320, doi:10.1029/RS025i006p01311.
- Papadopoulos, K., T. Wallace, G. M. Milikh, W. Peter, and M. McCarrick (2005), The magnetic response of the ionosphere to pulsed HF heating, *Geophys. Res. Lett.*, 32, L13101, doi:10.1029/2005GL023185.
- Papadopoulos, K., B. Tesfaye, H. Shroff, X. Shao, G. Milikh, C. Chang, T. Wallace, U. Inan, and D. Piddychiy (2007), F-region magnetospheric ULF generation by modulated ionospheric heating, *Eos Trans. AGU*, 88(52), Fall Meet. Suppl., Abstract SM53D-04.
- Papadopoulos, K., N. A. Gumerov, X. Shao, I. Doxas, and C. L. Chang (2011a), HF-driven currents in the polar ionosphere, *Geophys. Res. Lett.*, 38, L12103, doi:10.1029/2011GL047368.
- Papadopoulos, K., C.-L. Chang, J. Labenski, and T. Wallace (2011b), First demonstration of HF-driven ionospheric currents, *Geophys. Res. Lett.*, 38, L20107, doi:10.1029/2011GL049263.
- Payne, J. A., U. S. Inan, F. R. Foust, T. W. Chevalier, and T. F. Bell (2007), HF modulated ionospheric currents, *Geophys. Res. Lett.*, 34, L23101, doi:10.1029/2007GL031724.
- Rastogi, R. G. (1989), The equatorial electrojet, in *Geomagnetism*, vol. 3, edited by J. Jacobs, pp. 461–525, Elsevier, New York.
- Rietveld, M. T., R. Barr, H. Kopka, E. Nielson, P. Stubbe, and R. L. Dowden (1984), Ionospheric heater beam scanning: A new technique for ELF studies of the auroral ionosphere, *Radio Sci.*, 19(4), 1069–1077, doi:10.1029/RS019i004p01069.
- Rietveld, M. T., H.-P. Mauelshagen, P. Stubbe, H. Kopka, and E. Nielsen (1987), The characteristics of ionospheric heating-produced ELF/VLF waves over 32 hours, *J. Geophys. Res.*, 92, 8707–8722, doi:10.1029/JA092iA08p08707.
- Rietveld, M. T., P. Stubbe, and H. Kopka (1989), On the frequency dependence of ELF/VLF waves produced by modulated ionospheric heating, *Radio Sci.*, 24(3), 270–278, doi:10.1029/RS024i003p00270.
- Rishbeth, H. (1997), The ionospheric E-layer and F-layer dynamos—A tutorial review, *J. Atmos. Sol. Terr. Phys.*, 59(15), 1873–1880, doi:10.1016/S1364-6826(97)00005-9.
- Tepley, L., and R. K. Landshoff (1966), Waveguide theory for ionospheric propagation of hydromagnetic emissions, *J. Geophys. Res.*, 71(5), 1499–1504, doi:10.1029/JZ071i005p01499.
- Uman, M. A. (1987), *The Lightning Discharge*, Int. Geophys. Ser., vol. 39, edited by W. L. Donn, Academic, New York.